

On the Drivers of Temperature Extremes on the Antarctic Peninsula During Austral Summer

Sai Wang (✉ wangs@cma.gov.cn)

China Academy of Meteorological Sciences <https://orcid.org/0000-0002-4648-0439>

Minghu Ding

China Academy of Meteorological Sciences

Ge Liu

China Academy of Meteorological Sciences

Ting Wei

China Academy of Meteorological Sciences

Wenqian Zhang

China Academy of Meteorological Sciences

Wen Chen

Institute of Atmospheric Physics Chinese Academy of Sciences

Tingfeng Dou

University of the Chinese Academy of Sciences

Cunde Xiao

Beijing Normal University

Research Article

Keywords: temperature extremes, Antarctic Peninsula, temperature advection, Rossby wave trains

Posted Date: February 23rd, 2021

DOI: <https://doi.org/10.21203/rs.3.rs-221785/v1>

License:  This work is licensed under a Creative Commons Attribution 4.0 International License.

[Read Full License](#)

23 Corresponding author*:

24 Prof. Minghu Ding,

25 State Key Laboratory of Severe Weather and Institute of Tibetan Plateau & Polar

26 Meteorology,

27 Chinese Academy of Meteorological Sciences, Beijing, China

28 Email: dingminghu@foxmail.com

29

30

31

32

33

34

35

36

37

38

39

40

41

42

43

44

45 **Abstract**

46 On the basis of surface air temperature (SAT) observations from the Great Wall
47 Station located on the Antarctic Peninsula (AP) and ERA-Interim reanalysis data, the
48 present manuscript investigates the role of atmospheric flow at intraseasonal and
49 synoptic time scales in driving the temperature extremes over the AP during austral
50 summer. Both warm and cold events can persist for multiple days and were maintained
51 mainly by the advection of seasonal air temperature by intraseasonal winds. Synoptic
52 winds can influence the temperature change around the peak time through their
53 advection of seasonal temperature, thus determining the time of peak temperature
54 anomalies. The generation of intraseasonal winds was closely associated with Rossby
55 wave trains propagating along the polar front jet over the Atlantic sector of the Southern
56 Ocean before the warm and cold events. The synoptic height anomalies before the warm
57 events were also manifested as Rossby wave trains propagating along the polar front
58 jet. However, synoptic Rossby wave trains were almost absent when the cold events
59 occurred. Further analysis indicates that the weakened background flow during the cold
60 events may have hindered the eastward travel of synoptic eddies. This study provides
61 an important guidance for subseasonal to seasonal prediction on the AP.

62 **Key words:** temperature extremes, Antarctic Peninsula, temperature advection, Rossby
63 wave trains

67 **1. Introduction**

68 Variations in surface air temperature (SAT) may have pronounced impacts on
69 glaciological, oceanographic, chemical and biological processes in the Antarctic and
70 surrounding ocean areas (Scambos et al. 2000; Cook et al. 2005; Meredith and King
71 2005; Turner et al. 2017). As revealed by satellite images, the surface melting induced
72 by an increase in SAT was the dominant process leading to the disintegration and
73 collapse of ice shelves (Scambos et al. 2000; Fahnestock et al. 2002; Cook et al. 2005).
74 Furthermore, the variations in SAT can impact the biological processes in the
75 surrounding ocean areas. For example, the increase in SAT and resulting sea ice loss
76 along the western Antarctic Peninsula (AP) have led to an increase in competition
77 among krill-eating predators (Trivelpiece et al. 2011). Therefore, it is important to
78 investigate the mechanisms that drive Antarctic SAT variability.

79 Because the western AP is one of the regions experiencing the most warming on
80 the planet, the SAT variability over the western AP has recently gained increasing
81 attention (Turner et al. 2005; Marshall et al. 2006; Turner et al. 2016; Jones et al. 2019).
82 During the austral autumn, winter, and spring seasons, apparent warming signals have
83 occurred over the western AP (King 1994; Turner et al. 2005; Ding and Steig 2013;
84 Clem and Fogt 2015) related to tropical Pacific forcing during autumn. Autumn tropical
85 Pacific forcing was suggested to deepen the Amundsen/Bellingshausen Sea low (ASL),
86 which can reduce sea ice along the western AP coast and advect warmer air to the AP
87 (Ding and Steig 2013). According to Li et al. (2014), wintertime sea surface warming
88 related to the Atlantic Multidecadal Oscillation can also deepen the ASL, further

89 contributing to the warming trend over the AP. During austral summer, a warming trend
90 can be observed on the northeastern AP (Turner et al. 2005; Orr et al. 2008).
91 Summertime warming can be partly attributed to the positive trend in the Southern
92 Annular Mode (SAM) (Orr et al. 2004; Marshall et al. 2006), which is induced by
93 stratospheric ozone depletion and increasing greenhouse gas concentrations (Thompson
94 et al. 2002; Marshall and Gareth 2003; Arblaster and Meehl 2006; Thompson et al.
95 2011). Since the late 1990s, an apparent decrease in SAT on the AP has occurred, which
96 is due to natural variability (Hawkins et al. 2016; Turner et al. 2016; Ding et al., 2020).

97 The temperature over the AP is characterized by large interannual variability,
98 especially over the western AP (Marshall et al. 2006; Clem and Fogt 2013). According
99 to previous studies, the change in the phase of the SAM can exert the greatest control
100 on the interannual variability in SAT across the AP (Marshall and Thompson 2016;
101 Turner et al. 2020). When the SAM is its positive (negative) phase, an increase
102 (decrease) in the temperature can be observed across the AP (Marshall and Thompson
103 2016). The variations in the phase of the El Niño-Southern Oscillation (ENSO) and the
104 associated tropical Pacific-high latitude teleconnection can also influence winter
105 temperatures on the AP (Marshall and King 1998; Clem et al. 2016; Clem et al. 2017).
106 Furthermore, the magnitude of the teleconnection is modulated by the magnitude and
107 phase of the SAM (Fogt et al. 2011). Significant teleconnections can be observed only
108 when ENSO events occur with a weak SAM or when ENSO is in phase with the SAM.

109 The aforementioned efforts have helped to improve our understanding of the
110 mechanisms of climate variability on the AP from interannual to multidecadal time

111 scales. However, there is still a general lack of investigation about the mechanisms of
112 extreme temperature events on the AP. In fact, weather or climate extremes could have
113 a large influence on the Antarctic cryosphere and ecosystems. Investigating the
114 dynamic mechanisms governing extreme temperatures on the AP can improve our
115 understanding of the climate variability on the AP. Furthermore, revealing the
116 precursory signals of extreme temperatures on the AP can provide important guidance
117 for the subseasonal prediction of the climate variability in the region, which is one aim
118 of the Polar Prediction Project (Jung et al., 2016). The main goal of this study is to
119 investigate the dynamic mechanisms governing summertime extreme warm and cold
120 temperatures on the AP. The rest of the paper is organized as follows: the observational
121 and reanalysis data and methods used in this study are introduced in Sect. 2. The results
122 are presented in Sect. 3. Sect. 4 provides a summary.

123

124 **2. Data and methods**

125 The present study employs the SAT from the Great Wall Station ($62^{\circ}13'S$, $58^{\circ}58'W$;
126 WMO ID: 89058), which is located on the Fildes Peninsula of King George Island. The
127 daily SAT is obtained by calculating the average value of observations taken at six-hour
128 intervals (0000, 0600, 1200 and 1800 UTC). This study also employs the daily
129 horizontal wind, air temperature, geopotential height, vertical motion at different
130 pressure levels, sea level pressure (SLP) and SAT data from the European Centre for
131 Medium-Range Weather Forecasts (ECMWF) ERA-Interim reanalysis (Dee et al. 2011).
132 The atmospheric data from ERA-Interim reanalysis have a horizontal resolution of 2.5°

133 $\times 2.5^\circ$ and are available for 1979 to 2018.

134 Extreme warm (cold) events are identified as when the normalized SAT values at
135 the Great Wall Station exceed 1 (-1) standard deviation and persist for longer than or
136 equal to 3 days. Since the present study mainly focuses on persistent warm and cold
137 events, the threshold is selected as durations greater than or equal to 3 days. It should
138 be noted that the obtained results do not change for other similar thresholds, such as 5
139 days. The day when the normalized SAT values reach the maximum is taken as a
140 reference (lag 0 day). Composite analysis is performed to obtain the common features
141 of the extreme events during the 1985/86 to 2017/18 summers. According to our
142 definition of extreme temperature events, 42 warm events and 48 cold events are
143 identified during the period of 1986–2018 (Tables 1, 2).

144 The present study extracts synoptic, intraseasonal and seasonal variations from the
145 original field using Butterworth high-pass (shorter than 8 days), bandpass (8–90 days)
146 and low-pass (longer than 90 days) filters. The weights of the Lanczos filters are 17 for
147 synoptic variations and 181 for intraseasonal and seasonal variations. The storm track
148 activity is represented by the root mean square of the 2–8 day bandpass filtered 300-
149 hPa meridional wind (Wang et al. 2020b; Wang et al. 2020c). In the present study, the
150 temperature tendency equation is used to reveal the dynamic mechanisms driving the
151 temperature anomalies. The temperature tendency equation is written as:

152
$$\frac{\partial T}{\partial t} = -\vec{V} \cdot \nabla T + S_p \omega + Q, (1)$$

153 where T is the temperature, \vec{V} is the horizontal velocity, $S_p = -\frac{T}{\theta} \frac{\partial \theta}{\partial P}$ is the static
154 stability for which θ is the potential temperature, and $\omega = \frac{dP}{dt}$ is the vertical motion.

155 The first term on the right-hand side (r.h.s.) is the horizontal temperature advection; the
 156 second term accounts for the adiabatic heating contribution; Q represents the remaining
 157 diabatic heating contribution. The horizontal temperature advection and adiabatic
 158 heating terms at the surface are calculated following the method of Lee et al. (2011).
 159 To evaluate the contribution of atmospheric flow at different time scales in driving the
 160 temperature anomalies, the advection term in the temperature tendency equation is
 161 decomposed following the method of Song et al. (2018): First, any variable such as A
 162 can be decomposed as:

$$A = A^S + A^L + A^H, \quad (2)$$

164 where the superscripts S, L and H denote the seasonal, intraseasonal and synoptic
 165 components. Thus, the advection terms associated with the intraseasonal oscillations
 166 (ISOs), synoptic variations and mixture of the ISOs and synoptic variations can
 167 respectively be expressed as:

$$\begin{aligned} & u^L \frac{\partial T^L}{\partial x} + u^L \frac{\partial T^S}{\partial x} + u^S \frac{\partial T^L}{\partial x} + v^L \frac{\partial T^L}{\partial y} + v^L \frac{\partial T^S}{\partial y} + v^S \frac{\partial T^L}{\partial y}; \\ & u^H \frac{\partial T^H}{\partial x} + u^H \frac{\partial T^S}{\partial x} + u^S \frac{\partial T^H}{\partial x} + v^H \frac{\partial T^H}{\partial y} + v^H \frac{\partial T^S}{\partial y} + v^S \frac{\partial T^H}{\partial y}; \\ & u^L \frac{\partial T^H}{\partial x} + u^H \frac{\partial T^L}{\partial x} + v^L \frac{\partial T^H}{\partial y} + v^H \frac{\partial T^L}{\partial y}, \quad (3) \end{aligned}$$

171 The present study also employs the wave activity flux proposed by Takaya and
 172 Nakamura (2001) to illustrate the propagation of atmospheric stationary Rossby waves.
 173 Two-tailed Student's t test is used to evaluate the statistical significance of the
 174 composite analysis.

175

176 3. Results

177 **3.1 The evolution of SAT anomalies**

178 Figures 1a and b display the evolution of the composite SAT anomalies at the Great
179 Wall Station during the lag -10 to lag +10 days of warm and cold events, respectively.
180 For the warm events, the temperature anomalies at the Great Wall Station were above
181 0 °C from day -10 to day +10 (Fig. 1a). However, the magnitudes of the temperature
182 anomalies were relatively small from day -10 to day -4 and from day +4 to day +10
183 (Fig. 1a). After day -4, the temperature anomalies increased rapidly and reached the
184 peak value on lag 0 day (Fig. 1a). After the peak time (day 0), the temperature anomalies
185 decayed rapidly from day 0 to day +4 and returned to small positive values on day +4
186 (Fig. 1a). For the cold events, anomalies with opposite signs are observed. During the
187 periods of lag -10 to lag -4 days and lag +4 to lag +10 days, small negative values of
188 SAT anomalies can be observed (Fig. 1b). During lag -4 to lag 0 days, the temperature
189 anomalies declined rapidly and reached the lowest value on lag 0 day. The temperature
190 anomalies recovered to small negative values during lag 0 to lag +4 days. By
191 comparison, the magnitude of the peak temperature anomaly of the cold events
192 (approximately 3 °C) is larger than that of the warm events (less than 3 °C).

193 Next, the spatiotemporal evolution of SAT anomalies for the warm and cold events
194 is assessed. On day -4 of the warm events, weak but significant warm anomalies can be
195 observed over the region of the Drake Passage (Fig. 2a). Then, both the spatial coverage
196 and magnitude of the warming anomalies increased. On day -2, the warm anomalies
197 expanded southward to the AP region (Fig. 2b). Meanwhile, significant cold anomalies
198 appeared over the Amundson Sea (Fig. 2b). From lag -2 to lag 0 days, both the warm

199 and cold anomalies increased gradually and reached their peak values on day 0 (Figs.
200 2b, c). On day +2, the warm anomalies over the Drake Passage and the cold anomalies
201 over the Amundson Sea weakened (Fig. 2d). On day -4 of cold events, significant cold
202 anomalies covered the southern part of South America, the Drake Passage and the
203 northern part of the AP (Fig. 2e). On day -2, the cold anomalies expanded southward to
204 the whole peninsula and were sustained to day +2 (Figs. 2f-h). On day 0, the cooling
205 anomalies reached their peak values, and the maximum of the cold anomalies was
206 located on the northern part of the AP (Fig. 2g), corresponding to the peak value of SAT
207 anomalies at the Great Wall Station.

208 Next, the synoptic, intraseasonal, and seasonal components of the temperature
209 anomalies at the Great Wall Station are extracted to quantitatively evaluate the
210 contributions to the variations in temperature at different time scales. As displayed in
211 Figure 3, the contributions to temperature anomalies at different time scales varied in
212 different periods. The seasonal temperature anomaly during the lifetime of the warm
213 (cold) events maintained a stable value of approximately 0.48 °C (-0.56 °C), which
214 made the largest contribution to the total temperature anomaly from day -10 to day -4
215 and from day +4 to day +10 (Fig. 3). During lag -3 to lag +3 days, the intraseasonal
216 temperature anomaly accounted for the majority of the total temperature anomalies,
217 indicating the importance of the ISOs to the occurrence and strength of the temperature
218 events (Fig. 3). On the peak day, the magnitudes of the synoptic temperature anomalies
219 were second only to those of the intraseasonal temperature anomalies (Fig. 3),
220 indicating the important role of the synoptic temperature anomalies in influencing the

221 peak time of temperature anomalies.

222 Figures 4 and 5 display the spatiotemporal evolutions of SAT anomalies induced
223 by intraseasonal, synoptic and seasonal variations for the warm events and cold events,
224 respectively. As shown in Figures 4a-d, the spatial pattern of the temperature anomalies
225 due to the ISOs is very similar to that of the original anomalies from lag -4 to lag +2
226 days. Furthermore, their magnitude made the largest contribution to the original
227 anomalies. For the synoptic temperature, significant warm anomalies over the Drake
228 Passage can be observed only on day 0 (Fig. 4g). On day +2, the warm anomalies
229 associated with the synoptic variations over the Drake Passage were replaced by cold
230 anomalies (Fig. 4h). For the seasonal component, stable warm anomalies can be
231 observed over the Drake Passage (Figs. 4i-l), which implies that persistent warm events
232 are likely to occur during a warmer summer. During lag -4 to lag +2 days, the
233 magnitudes of synoptic and seasonal temperature anomalies over the Drake Passage
234 were smaller than those of intraseasonal anomalies, which indicates the dominant
235 contribution of ISOs to the total temperature anomalies. For the cold events, the spatial
236 pattern of the ISO-induced temperature anomalies was also very similar to that of the
237 original anomalies during the lifetime of the cold events (Fig. 5). Furthermore, seasonal
238 temperature anomalies may provide favourable conditions for the occurrence of
239 persistent cold events (Figs. 5i-l). The SAT anomalies induced by synoptic variations
240 can only account for the cooling anomalies over the northern part of the AP on day 0 of
241 the cold events (Fig. 5g). By comparison, the ISO-induced temperature anomalies made
242 the dominant contribution to the total temperature anomalies during lag -4 to lag +2

243 days of the cold events (Fig. 5).

244

245 **3.2 Diagnostic analysis of SAT anomalies**

246 According to the above analysis, the temporal evolutions of SAT anomalies of the
247 extreme temperature events at the Great Wall Station are closely related to the
248 development of SAT anomalies over the Drake Passage region (70°S – 50°S and 80°W –
249 50°W). To explore the influence of the anomalous atmospheric flow on the SAT
250 anomalies, the contributions of the horizontal advection term and diabatic heating term
251 are assessed first in this section. Figure 6 displays the composite anomalies of SAT and
252 the tendency of the SAT anomalies averaged over the Drake Passage region during lag
253 -5 to lag +5 days of the warm and cold events. The evolution of the composite SAT
254 anomalies over the Drake Passage region based on the ERA-Interim data matches well
255 with the observed SAT anomalies at the Great Wall Station. As shown in Figures 6a and
256 d, the regionally averaged temperature anomalies (black line) increase in magnitude
257 from day -5 to day 0 and reach the peak value on lag 0 day. After the peak (day 0), the
258 temperature anomalies decay from day 0 to day +5 (Figs. 6a, d). The tendency of the
259 observed air temperature anomalies (red line) is positive from lag -5 to lag 0 days of
260 the warm events (Fig. 6a), which corresponds well to the increase in the warm
261 anomalies over the Drake Passage region. After day 0, the regionally averaged values
262 of the temperature tendency become negative (Fig. 6a), which corresponds to the decay
263 of the warm anomalies over the Drake Passage. For the cold events, the composite SAT
264 tendency is negative overall before lag 0 day (Fig. 6d), corresponding to the

265 enhancement of the cold anomalies over the Drake Passage region. After the peak day
266 (day 0), the observed tendency of temperature turns positive, indicating the weakening
267 of the cold anomalies (Fig. 6f). According to Figure 6b, the horizontal advection term
268 facilitates the development of the warm anomalies during lag -4 to lag +4 days of the
269 warm events. The diabatic heating term can only act to weakly impede the growth of
270 the warm anomalies from lag -1 to lag +3 days (Fig. 6b). At the developing stage of the
271 warm events (lag -4 to lag 0 days), the positive temperature tendency induced by the
272 horizontal advection term is overall larger than the observed tendencies (Fig. 6b). This
273 implies that the development and maintenance of the warm anomalies was mainly
274 induced by the horizontal advection term, whereas the adiabatic heating term may have
275 made the dominant contribution in impeding the growth of the warm anomalies.
276 Similarly, the development and maintenance of the cold anomalies was also mainly
277 induced by the horizontal advection term (Fig. 6e).

278 To shed light on the role of atmospheric flow at intraseasonal and synoptic time
279 scales in inducing temperature anomalies, the temperature tendency induced by
280 different parts of the advection term is further examined. In Figure 6c, the advection
281 term associated with the ISOs evolves slowly and maintains a positive value larger than
282 those of the other two terms from lag -5 to lag +4 days. This suggests the important role
283 of the ISOs in sustaining the duration of the warm events. From day -2 to day +1, the
284 advection term associated with the synoptic variations was positive and made a non-
285 negligible contribution to the advection term on day 0 (Fig. 6c). This indicates that the
286 synoptic variations are important to the temperature increase around the peak time. The

287 ISOs also played an important role in sustaining the duration of temperature events (Fig.
288 6f). The advection term associated with the synoptic variations was negative from day
289 -2 to day +1 (Fig. 6f), decreasing the temperature around the peak time of the cold
290 events. During the lifetimes of both the warm and cold events, the tendencies induced
291 by the mixed terms were small, indicating their limited contributions to the evolution
292 of SAT.

293 Figure 7 shows different parts of the advection terms associated with the ISOs and
294 synoptic variations on lag 0 days of the warm and cold events. After decomposing the
295 advection term, it is found that the term $v^L \frac{\partial T^S}{\partial y}$ was the primary contributor to the
296 positive anomalies of tendency on lag 0 day of the warm events, whereas the term
297 $v^H \frac{\partial T^S}{\partial y}$ played a secondary role in inducing the positive anomalies of tendency (Figs.
298 7a, b). Therefore, the development of warm anomalies over the Drake Passage around
299 the peak time was mainly induced by the meridional advection of seasonal air
300 temperature by intraseasonal and synoptic meridional wind anomalies. For the cold
301 events, the term $v^L \frac{\partial T^S}{\partial y}$ acted as the primary contributor to the maintenance of cold
302 anomalies (Fig. 7c). In addition, the terms $u^L \frac{\partial T^S}{\partial x}$ and $v^H \frac{\partial T^S}{\partial y}$ also made non-
303 negligible contributions to the cooling tendency (Figs. 7c, d). In general, intraseasonal
304 and synoptic wind anomalies are vital to the formation of temperature anomalies around
305 the peak time of temperature events.

306

307 **3.3 The associated atmospheric circulation anomalies**

308 The above analysis indicates the important role of intraseasonal and synoptic wind

309 anomalies in inducing temperature tendency anomalies. This section assesses the
310 detailed evolution of atmospheric circulation anomalies. Figure 8 displays the
311 composite anomalies of the intraseasonal components of SLP and surface horizontal
312 wind during lag -4 to lag + 2 days of the warm and cold events. On lag -4 day of the
313 warm events, an anomalous cyclone can be observed west of the Drake Passage (Fig.
314 8a). The northerly (southerly) wind anomalies prevailed on the cyclone's east (west)
315 side (Fig. 8a), facilitating the advection of warm (cold) air from low (high) latitudes
316 and the formation of warm (cold) anomalies. On day -3, an anomalous anticyclone
317 formed east of the Drake Passage (Fig. 8b). The collocation of the anomalous cyclone
318 west of the Drake Passage and the anticyclone east of the Drake Passage can lead to
319 warm anomalies over the region of the Drake Passage. The SLP and wind anomalies
320 due to the ISOs increased in their magnitudes gradually from lag -4 to 0 days (Figs. 8a,
321 c), which corresponds well to the increase in warm anomalies over the Drake Passage.
322 On day +2 of the warm events, the anomalous cyclone west of the Drake Passage
323 weakened (Fig. 8d), which can explain the decrease in the temperature tendency
324 induced by ISOs. During lag -4 to lag +2 days of the cold events, the composite pattern
325 of SLP anomalies due to the ISOs is characterized by an anomalous anticyclone over
326 the Bellingshausen Sea and an anomalous cyclone east of the Drake Passage (Figs. 8e-
327 h). Under the influence of the dipole pattern, southeasterly wind anomalies prevailed
328 over the region of the Drake Passage, which can lower the temperature through
329 advection of the seasonal SAT. The magnitudes of ISO-induced SLP and southeasterly
330 wind anomalies intensified from lag -4 to lag 0 days (Figs. 8e-g). As a result, the

331 negative anomalies of the temperature tendency increased in magnitude, which is
332 conducive to the development and maintenance of cooling anomalies over the region
333 of the Drake Passage, including the AP. On day +2, the weakening of the intraseasonal
334 SLP and wind anomalies led to a decrease in the magnitudes of advection terms
335 associated with the ISOs (Fig. 8h).

336 Figure 9 displays the composite anomalies of the synoptic component of SLP and
337 surface horizontal wind during lag -2 to lag +1 days of the warm and cold events.
338 Different from the SLP anomalies due to ISOs, apparent eastward propagation of
339 synoptic SLP anomalies can be observed during the lifetime of the temperature events.
340 On lag -2 day of the warm events, an anomalous cyclone appeared over the Amundson
341 Sea (Fig. 9a). The anomalous cyclone moved to the Bellingshausen Sea on lag -1 day
342 (Fig. 9b). Meanwhile, an anomalous anticyclone can be observed east of the anomalous
343 cyclone (Fig. 9b). On the peak day of the warm events, the anomalous cyclone
344 (anticyclone) moved into the region east (west) of the Drake Passage (Fig. 9c). Under
345 the influence of the synoptic SLP pattern, warm air can be advected to the Drake
346 Passage by the northerly wind anomalies, producing positive values of temperature
347 anomalies. On day +1, the collapse of the synoptic cyclone west of the Drake Passage
348 and ongoing eastward movement of the synoptic anticyclone east of the Drake Passage
349 destroyed the favourable conditions for the increase in synoptic temperature over the
350 Drake Passage (Fig. 9d). For the cold events, apparent synoptic SLP anomalies can be
351 observed only around the peak day of the cold events. On lag 0 day, a small-scale
352 anomalous cyclone appeared over the Weddell Sea (Fig. 9g). The synoptic circulation

353 pattern was conducive to the advection of cold air to the southern edge of the AP.
354 However, no anomalous anticyclone appeared upstream or downstream of the
355 anomalous cyclone.

356 Next, the spatiotemporal evolution of upper tropospheric (300 hPa) circulation
357 anomalies are assessed. Figure 10 displays the intraseasonal component of 300-hPa
358 geopotential height anomalies and associated wave activity flux during lag -6 to lag 0
359 days of the warm and cold events. The composite pattern of the intraseasonal height
360 anomalies for the warm and cold events are both manifested as a Rossby wave train
361 propagating along the polar jet over the Atlantic Sector of the Southern Ocean. On lag
362 -6 days of the warm events, an anticyclonic centre can be observed east of New Zealand
363 (Fig. 10a). Due to the southeastward propagating stationary Rossby wave packet
364 emanating from the anticyclonic centre east of New Zealand, cyclonic anomalies
365 formed and developed over the Amundsen/Bellingshausen Sea (ABS) (Figs. 10a, b).
366 The cyclonic anomalies over the ABS intensified and further triggered eastward
367 propagating stationary Rossby waves, leading to the formation of anticyclonic
368 anomalies east of the Drake Passage on day -2 (Fig. 10c). On the peak day of the warm
369 events, the action centres east of the Drake Passage gradually amplified with continuous
370 eastward propagation of wave activity fluxes (Fig. 10d). However, the magnitude of the
371 anticyclonic centre east of New Zealand weakened on day 0 (Fig. 10d). On day -6 of
372 the cold events, an intraseasonal wave train can be observed, with anticyclonic centres
373 over New Zealand and cyclonic centres over the region east of New Zealand (Fig. 10e).
374 Due to the ongoing eastward propagation of wave activity fluxes emanating from New

375 Zealand, anticyclonic anomalies over the Bellingshausen Sea and cyclonic anomalies
376 east of the Drake Passage formed and intensified (Figs. 10e-h). On day 0, the magnitude
377 of the cyclonic anomalies east of the Drake Passage reached its peak values (Fig. 10h),
378 which correspond well with the peak values of SAT over the Drake Passage. However,
379 the magnitude of the upstream geopotential height anomalies weakened, as did the
380 associated wave activity fluxes (Fig. 10h).

381 Figure 11 displays the synoptic component of 300-hPa geopotential height
382 anomalies and associated wave activity flux for the warm and cold events. During the
383 lifetime of the warm events, the composite pattern of synoptic height anomalies
384 displayed a wave train pattern along the band within 50°S–60°S (Figs. 11a-d). Unlike
385 intraseasonal Rossby waves, synoptic Rossby waves are characterized by short
386 wavelengths and fast propagation speeds, which can explain the large mobility of
387 surface circulation and temperature anomalies on the synoptic time scale. However, no
388 apparent synoptic Rossby wave train can be observed from day -2 to day +1 of the cold
389 events (Figs. 11e-h). A natural question is why synoptic Rossby waves were absent
390 during the lifetime of the cold events. Previous studies have indicated that synoptic
391 eddies are steered by upper-level winds (Wallace et al. 1988; Chang and Yu 1999;
392 Wang et al. 2020a; Wang et al. 2021). The weaker zonal wind may hinder the eastward
393 propagation of synoptic eddies from the region. Therefore, it is hypothesized that the
394 absence of synoptic Rossby wave trains is due to weak background westerlies. The
395 following evidence is presented to confirm the hypothesis. Figure 12 displays the
396 composite anomalies of the seasonal component of 300-hPa zonal wind and storm track

397 activity when the extreme cold events occurred. As the seasonal component of zonal
398 wind and storm track activity did not vary much within a few days, we display only the
399 seasonal component of zonal wind and storm track activity on day 0 of the cold events.
400 As shown in Figure 12a, remarkable weakening of the 300-hPa zonal wind can be
401 observed over the Drake Passage. Under the influence of the background flow, fewer
402 synoptic eddies can propagate from the ABS to the Drake Passage, which is expressed
403 as a decrease in the storm track activity along 60°S (Fig. 12b). The synoptic SLP and
404 surface wind anomalies around the peak time of the cold events are probably induced
405 by the local cyclone.

406

407 **4. Summary**

408 On the basis of observational SAT from the Great Wall Station, the present study
409 identified 42 warm events and 48 cold events over the AP during the 1985/86 to
410 2017/18 summers. It was found that the temporal evolutions of SAT anomalies during
411 the lifetimes of the warm and cold events were closely related to the development of
412 SAT anomalies over the Drake Passage region. Further diagnostic analysis indicated
413 that the development of the SAT anomalies over the Drake Passage region during the
414 lifetimes of the warm and cold events was induced mainly by the horizontal advection
415 term. Then, it was revealed that the advection terms induced by ISOs made the largest
416 contribution to sustaining the temperature extremes. The advection terms associated
417 with synoptic variations were found to make non-negligible contributions to the
418 formation and development of temperature anomalies around the peak time of

419 temperature events, indicating their important role in determining the time when the
420 temperature anomalies peak.

421 As illustrated in Figure 13, the atmospheric flow at intraseasonal and synoptic time
422 scales plays an important role in the formation of both the warm and cold events. The
423 advection terms associated with ISOs and synoptic variations were mainly induced by
424 the advection of seasonal air temperature by intraseasonal and synoptic winds. The
425 prevailing intraseasonal northerly wind anomalies during the lifetime of the warm
426 events were accompanied by anomalous cyclones west of the Drake Passage and
427 anomalous anticyclones east of the Drake Passage, which were parts of the
428 intraseasonal Rossby wave train propagating along the polar front jet over the Atlantic
429 Sector of the Southern Ocean. Before the warm events, the intraseasonal Rossby wave
430 packet emanating from the anticyclonic centre east of New Zealand led to the formation
431 and development of cyclonic anomalies over the ABS and anticyclonic anomalies east
432 of the Drake Passage. For the cold events, the positive SLP anomalies over the
433 Bellingshausen Sea and negative anomalies east of the Drake Passage and associated
434 southeasterly wind anomalies were also closely related to the intraseasonal wave train
435 propagating along the polar front jet. The ongoing eastward propagation of wave
436 activity fluxes emanating from anticyclonic centres over New Zealand was suggested
437 to induce the formation and development of anticyclonic anomalies over the
438 Bellingshausen Sea and cyclonic anomalies east of the Drake Passage.

439 The synoptic variations associated with the development of the warm events
440 manifest as shorter and faster moving Rossby wave trains. In contrast, synoptic Rossby

441 wave trains cannot be observed during the lifetime of the cold events. Further analysis
442 indicated that the absence of the synoptic wave train was due to the weakened
443 background flow. A decrease in the seasonal zonal wind can be observed over the Drake
444 Passage when the cold events occurred, which may have hindered the eastward travel
445 of synoptic eddies. The synoptic anomalies of SLP and surface wind were assumed to
446 be induced by the local cyclone. Further analysis is needed to shed light on the role of
447 short-term cyclones in influencing climate change on the AP.

448

449 **Acknowledgements:**

450 This research was funded by the National Science Foundation of China (41771064),
451 the CN National Research and Development Projects, grant number 2019YFC1509100
452 and the Basic Research Fund of the Chinese Academy of Meteorological Sciences,
453 grant number 2019Z008. This is a contribution to the Year of Polar Prediction (YOPP),
454 a flagship activity of the Polar Prediction Project (PPP), initiated by the World Weather
455 Research Programme (WWRP) of the World Meteorological Organization (WMO).

456

457 **Conflicts of interest:**

458 The authors declare no potential conflicts of interest.

459

460

461

462

463 **Reference:**

464 Arblaster JM, Meehl GA (2006) Contributions of External Forcings to Southern
465 Annular Mode Trends. *Journal of Climate* 19:2896-2905

466 Chang EKM, Yu DB (1999) Characteristics of Wave Packets in the Upper Troposphere.
467 Part I: Northern Hemisphere Winter. *Journal of the Atmospheric Sciences*
468 42:1708-1728

469 Clem KR, Fogt RL (2013) Varying roles of ENSO and SAM on the Antarctic Peninsula
470 climate in austral spring. *Journal of Geophysical Research: Atmospheres*
471 118:11,481-411,492. <https://doi.org/10.1002/jgrd.50860>

472 Clem KR, Fogt RL (2015) South Pacific circulation changes and their connection to the
473 tropics and regional Antarctic warming in austral spring, 1979–2012. *Journal of*
474 *Geophysical Research: Atmospheres* 120:2773-2792.
475 <https://doi.org/10.1002/2014jd022940>

476 Clem KR, Renwick JA, Mcgregor J (2017) Large-Scale Forcing of the Amundsen Sea
477 Low and Its Influence on Sea Ice and West Antarctic Temperature. *Journal of*
478 *Climate* 30:8405-8424

479 Clem KR, Renwick JA, Mcgregor J, Fogt RL (2016) The relative influence of ENSO
480 and SAM on Antarctic Peninsula climate. *Journal of Geophysical Research:*
481 *Atmospheres* 121:9324-9341

482 Cook AJ, Fox AJ, Vaughan DG, Ferrigno JG (2005) Retreating glacier fronts on the
483 Antarctic Peninsula over the past half-century. *Science* 308:541-544.
484 <https://doi.org/10.1126/science.1104235>

485 Dee DP et al. (2011) The ERA-Interim reanalysis: configuration and performance of
486 the data assimilation system. Quarterly Journal of the Royal Meteorological
487 Society 137:553-597. <https://doi.org/10.1002/qj.828>

488 Ding M, Han W, Zhang T, Yue X, Fyke J, Liu G, Xiao C (2020) Towards More Snow
489 Days in Summer since 2001 at the Great Wall Station, Antarctic Peninsula: The
490 Role of the Amundsen Sea Low. Advances in Atmospheric Sciences 37: 494-504.

491 Ding Q, Steig EJ (2013) Temperature Change on the Antarctic Peninsula Linked to the
492 Tropical Pacific*. Journal of Climate 26:7570-7585.
493 <https://doi.org/10.1175/jcli-d-12-00729.1>

494 Fahnestock MA, Abdalati W, Shuman CA (2002) Long melt seasons on ice shelves of
495 the Antarctic Peninsula: an analysis using satellite-based microwave emission
496 measurements. Annals of Glaciology, 34: 127-133.
497 doi:10.3189/172756402781817798

498 Fogt RL, Bromwich DH, Hines KM (2011) Understanding the SAM influence on the
499 South Pacific ENSO teleconnection. Climate Dynamics 36:1555-1576

500 Hawkins E, Smith RS, Gregory JM, Stainforth DA (2016) Irreducible uncertainty in
501 near-term climate projections. Climate Dynamics 46:3807-3819.
502 <https://doi.org/10.1007/s00382-015-2806-8>

503 Jones ME, Bromwich DH, Nicolas JP, Carrasco J, Plavcová E, Zou X, Wang S-H (2019)
504 Sixty Years of Widespread Warming in the Southern Middle and High Latitudes
505 (1957–2016). Journal of Climate 32:6875-6898. [https://doi.org/10.1175/jcli-d-](https://doi.org/10.1175/jcli-d-18-0565.1)
506 [18-0565.1](https://doi.org/10.1175/jcli-d-18-0565.1)

507 Jung T, Gordon ND, Bauer P, Bromwich DH, Chevallier M, Day JJ, Dawson J., Doblus-
508 Reyes F, Fairall C, Goessling HF, Holland M, Inoue J, Iversen T, Klebe S,
509 Lemke P, Losch M, Makshtas A, Mills B, Nurmi P, Perovich D, Reid P, Renfrew
510 IA, Smith G, Svensson G, Tolstykh M, Yang Q (2016) Advancing Polar
511 Prediction Capabilities on Daily to Seasonal Time Scales. *Bulletin of the*
512 *American Meteorological Society* 97: 1631-1647. doi: 10.1175/BAMS-D-14-
513 00246.1

514 King JC (1994) Recent climate variability in the vicinity of the antarctic peninsula.
515 *International Journal of Climatology* 14:357-369.
516 <https://doi.org/10.1002/joc.3370140402>

517 Lee S, Gong T, Johnson N, Feldstein SB, Pollard D (2011) On the Possible Link
518 between Tropical Convection and the Northern Hemisphere Arctic Surface Air
519 Temperature Change between 1958 and 2001. *Journal of Climate* 24:4350-4367

520 Li X, Holland DM, Gerber EP, Yoo C (2014) Impacts of the north and tropical Atlantic
521 Ocean on the Antarctic Peninsula and sea ice. *Nature* 505: 38–542.
522 <https://doi.org/10.1038/nature12945>

523 Marshall, Gareth J (2003) Trends in the Southern Annular Mode from observations and
524 reanalyses. *Journal of Climate* 14:4134-4143

525 Marshall GJ, King JC (1998) Southern hemisphere circulation anomalies associated
526 with extreme Antarctic peninsula winter temperatures. *Geophysical Research*
527 *Letters* 25:2437-2440. <https://doi.org/10.1029/98gl01651>

528 Marshall GJ, Orr A, van Lipzig NPM, King JC (2006) The Impact of a Changing

529 Southern Hemisphere Annular Mode on Antarctic Peninsula Summer
530 Temperatures. Journal of Climate 19:5388-5404.
531 <https://doi.org/10.1175/jcli3844.1>

532 Marshall GJ, Thompson DWJ (2016) The signatures of large-scale patterns of
533 atmospheric variability in Antarctic surface temperatures. Journal of
534 Geophysical Research-Atmospheres 121:3276-3289.
535 <https://doi.org/10.1002/2015jd024665>

536 Meredith MP, King JC (2005) Rapid climate change in the ocean west of the Antarctic
537 Peninsula during the second half of the 20th century. Geophysical Research
538 Letters 32: L19604. <https://doi.org/10.1029/2005gl024042>

539 Orr A, Cresswell D, Marshall GJ, Hunt JCR, Sommeria J, Wang CG, Light M (2004) A
540 'low-level' explanation for the recent large warming trend over the western
541 Antarctic Peninsula involving blocked winds and changes in zonal circulation.
542 Geophysical Research Letters 31: L06204.
543 <https://doi.org/10.1029/2003gl019160>

544 Orr A et al. (2008) Characteristics of Summer Airflow over the Antarctic Peninsula in
545 Response to Recent Strengthening of Westerly Circumpolar Winds. Journal of
546 the Atmospheric Sciences 65:1396-1413.
547 <https://doi.org/10.1175/2007jas2498.1>

548 Scambos TA, Hulbe C, Fahnestock M, Bohlander J (2000) The link between climate
549 warming and break-up of ice shelves in the Antarctic Peninsula. Journal of
550 Glaciology 46:516-530. <https://doi.org/10.3189/172756500781833043>

551 Song L, Wu R, Jiao Y (2018) Relative contributions of synoptic and intraseasonal
552 variations to strong cold events over eastern China. *Climate Dynamics* 50:
553 4619-4634. <https://doi.org/10.1007/s00382-017-3894-4>

554 Takaya K, Nakamura H (2001) A Formulation of a Phase-Independent Wave-Activity
555 Flux for Stationary and Migratory Quasigeostrophic Eddies on a Zonally
556 Varying Basic Flow. *Journal of Atmospheric Sciences* 58: 608-627

557 Thompson, David WJ, Solomon, Susan (2002) Interpretation of Recent Southern
558 Hemisphere Climate Change. *Science* 296: 895–899

559 Thompson DWJ, Solomon S, Kushner PJ, England MH, Grise KM, Karoly DJ (2011)
560 Signatures of the Antarctic ozone hole in Southern Hemisphere surface climate
561 change. *Nature Geoscience* 4:741-749

562 Trivelpiece WZ, Hinke JT, Miller AK, Reiss CS, Trivelpiece SG, Watters GM (2011)
563 Variability in krill biomass links harvesting and climate warming to penguin
564 population changes in Antarctica. *Proceedings of the National Academy of
565 Sciences of the United States of America* 108:7625-7628.
566 <https://doi.org/10.1073/pnas.1016560108>

567 Turner J et al. (2005) Antarctic climate change during the last 50 years. *International
568 Journal of Climatology* 25:279-294. <https://doi.org/10.1002/joc.1130>

569 Turner J et al. (2016) Absence of 21st century warming on Antarctic Peninsula
570 consistent with natural variability. *Nature* 535:411-415.
571 <https://doi.org/10.1038/nature18645>

572 Turner J, Marshall GJ, Clem K, Colwell S, Phillips T, Lu H (2020) Antarctic

573 temperature variability and change from station data. *International Journal of*
574 *Climatology* 40:2986-3007. <https://doi.org/10.1002/joc.6378>

575 Turner J, Orr A, Gudmundsson GH, Jenkins A, Bingham RG, Hillenbrand C-D,
576 Bracegirdle TJ (2017) Atmosphere-ocean-ice interactions in the Amundsen Sea
577 Embayment, West Antarctica. *Reviews of Geophysics* 55:235-276.
578 <https://doi.org/10.1002/2016rg000532>

579 Wallace JM, Lim G-H, Blackmon ML (1988) Relationship between Cyclone Tracks,
580 Anticyclone Tracks and Baroclinic Waveguides. *Journal of the Atmospheric*
581 *Sciences* 45:439-462. [https://doi.org/10.1175/1520-0469\(1988\)045<0439:](https://doi.org/10.1175/1520-0469(1988)045<0439:Rbctat>2.0.Co;2)
582 [Rbctat>2.0.Co;2](https://doi.org/10.1175/1520-0469(1988)045<0439:Rbctat>2.0.Co;2)

583 Wang S, Chen W, Chen S, Ding S (2020a) Interdecadal change in the North Atlantic
584 storm track during boreal summer around the mid-2000s: role of the
585 atmospheric internal processes. *Climate Dynamics* 55:1929-1944.
586 <https://doi.org/10.1007/s00382-020-05360-w>

587 Wang S, Chen W, Chen S, Nath D, Wang L (2020b) Anomalous winter moisture
588 transport associated with the recent surface warming over the Barents–Kara seas
589 region since the mid-2000s. *International Journal of Climatology* 40:2497-2505.
590 <https://doi.org/10.1002/joc.6337>

591 Wang S, Nath D, Chen W, Wang L (2020c) Changes in winter stationary wave activity
592 during weak mid-latitude and Arctic thermal contrast period. *International*
593 *Journal of Climatology* 40:1755-1768. <https://doi.org/10.1002/joc.6299>

594 Wang S, Nath D, Chen W (2021) Nonstationary relationship between sea ice over Kara–

595 Laptev seas during August–September and Ural blocking in the following
596 winter. International Journal of Climatology 41: E1608-E1622.

597 <https://doi.org/10.1002/joc.6794>

598

599

600

601

602

603

604

605

606

607

608

609

610

611

612

613

614

615

616

617

618

619

620

621

622

623

624

625

626

627

628

629

630

631

632

633

634

635

636 Table 1 The year and lag 0 day of the warm events. See the text for the definition of

637 warm events.

638

Year	Lag 0 day	Year	Lag 0 day
1985-1986	Feb 14	2002-2003	
1986-1987		2003-2004	
1987-1988	Feb 13; Feb 21	2004-2005	
1988-1989	Dec 30; Feb 25	2005-2006	Jan 4; Jan 18; Feb 7
1989-1990	Dec 29; Jan 19; Feb 13; Feb 27	2006-2007	Dec 4; Feb 11
1990-1991	Jan 12	2007-2008	Feb 24
1991-1992		2008-2009	Dec 19
1992-1993	Dec 2; Dec 24; Feb 11	2009-2010	
1993-1994		2010-2011	
1994-1995	Dec 5; Dec 17; Jan 21; Jan 24; Feb 11	2011-2012	
1995-1996	Feb 18	2012-2013	
1996-1997	Dec 21; Jan 14; Jan 24; Feb 14	2013-2014	
1997-1998	Jan 14	2014-2015	
1998-1999	Feb 24	2015-2016	
1999-2000	Dec 27	2016-2017	Dec 4; Feb 10
2000-2001	Feb 27	2017-2018	Dec 27; Feb 24
2001-2002	Dec 3; Dec 15; Jan 1		

639

640

641

642

643

644

645

646

647

648 Table 2 The year and lag 0 day of the cold events. See the text for the definition of

649 cold events.

650

Year	Lag 0 day	Year	Lag 0 day
1985-1986	Feb 18; Feb 28	2002-2003	Dec 4
1986-1987	Dec 8; Jan 10	2003-2004	Dec 6; Dec 18
1987-1988		2004-2005	Dec 16
1988-1989	Dec 2; Jan 23	2005-2006	Dec 7; Dec 20
1989-1990		2006-2007	Dec 24
1990-1991	Dec 2; Dec 14; Feb 22	2007-2008	
1991-1992	Dec 7; Dec 18; Dec 25; Feb 14; Feb 28	2008-2009	Feb 15
1992-1993		2009-2010	Dec 1; Jan 9; Jan 13; Jan 27; Feb 5; Feb 21
1993-1994	Feb 18	2010-2011	Dec 7; Jan 21
1994-1995		2011-2012	Feb 19
1995-1996		2012-2013	Dec 6; Jan 27
1996-1997		2013-2014	Jan 8; Feb 9
1997-1998	Dec 28	2014-2015	Feb 27
1998-1999		2015-2016	Jan 11; Jan 25; Feb 17
1999-2000		2016-2017	Feb 20
2000-2001	Jan 1; Feb 6; Feb 10; Feb 18; Feb 23	2017-2018	
2001-2002			

651

652

653

654

655

656

657

658

659

660

661 **Figure Captions:**

662

663 **Fig. 1** Time evolution of surface air temperature (SAT) anomalies ($^{\circ}\text{C}$) at the Great
664 Wall Station during lag -10 to lag +10 days of (a) warm and (b) cold events.

665 **Fig. 2** Composite SAT anomalies ($^{\circ}\text{C}$) on days (a) -4, (b) -2, (c) 0 and (d) +2 of the
666 warm events. (e)-(h) are the same as (a)-(d) but for cold events. The dots indicate
667 anomalies significant at the 95% confidence level. The green dot indicates the
668 location of the Great Wall Station.

669 **Fig. 3** The same as Fig. 1 but for the synoptic, intraseasonal, and seasonal components
670 of SAT.

671 **Fig. 4** Composite anomalies of the intraseasonal component of SAT ($^{\circ}\text{C}$) on days (a) -
672 4, (b) -2, (c) 0 and (d) +2 of the warm events. (e)-(h) and (i)-(l) are the same as (a)-(d)
673 but for the synoptic and seasonal components of SAT, respectively. The dots indicate
674 anomalies significant at the 95% confidence level. The green dot indicates the
675 location of the Great Wall Station.

676 **Fig. 5** The same as Fig. 4 but for the cold events.

677 **Fig. 6** Time evolution of the composite anomalies of (a) SAT (black line), SAT
678 tendency (red line), (b) SAT tendency induced by advection (red line) and adiabatic
679 (black line) terms and (c) SAT tendency caused by different parts of the advection
680 term averaged over the Drake Passage (70°S – 50°S and 80°W – 50°W) during lag -5 to
681 lag +5 days of the warm events. (d)-(f) are the same as (a)-(c) but for the cold events.

682 **Fig. 7** Different parts of advection terms associated with the (a), (c) ISOs and (b), (d)
683 synoptic variations on lag 0 day of the warm and cold events, respectively.

684 **Fig. 8** Composite anomalies of intraseasonal components of SLP (hPa) (shading) and
685 surface winds (ms^{-1}) (vectors) on days (a) -4, (b) -2, (c) 0 and (d) +2 of the warm
686 events. (e)-(h) are the same as (a)-(d) but for the cold events. The dots indicate
687 anomalies significant at the 95% confidence level.

688 **Fig. 9** Composite anomalies of synoptic components of SLP (hPa) (shading) and
689 surface winds (ms^{-1}) (vectors) on days (a) -2, (b) -1, (c) 0 and (d) +1 of the warm
690 events. (e)-(h) are the same as (a)-(d) but for the cold events. The dots indicate
691 anomalies significant at the 95% confidence level.

692 **Fig. 10** Composite anomalies of the intraseasonal component of geopotential height
693 anomalies at 300 hPa (m) (shading) and the attendant wave activity flux (vector) on
694 days (a) -6, (b) -4, (c) -2 and (d) 0 of the warm events. (e)-(h) are the same as (a)-(d)
695 but for the cold events. The dots indicate anomalies significant at the 95% confidence
696 level.

697 **Fig. 11** Composite anomalies of the synoptic component of geopotential height
698 anomalies at 300 hPa (m) (shading) and the attendant wave activity flux (vector) on
699 days (a) -2, (b) -1, (c) 0 and (d) +1 of the warm events. (e)-(h) are the same as (a)-(d)
700 but for the cold events. The dots indicate anomalies significant at the 95% confidence
701 level.

702 **Fig. 12** Composite anomalies of the seasonal component of (a) 300-hPa zonal wind
703 (ms^{-1}) and (b) 300-hPa storm track activity (m) for the cold events. The dots indicate
704 anomalies significant at the 95% confidence level.

705 **Fig. 13** Schematic illustration of the role of atmospheric flow in the formation

706 of summer temperature extremes at the Great Wall Station, Antarctic

707 Peninsula, during austral summer.

708

709

710

711

712

713

714

715

716

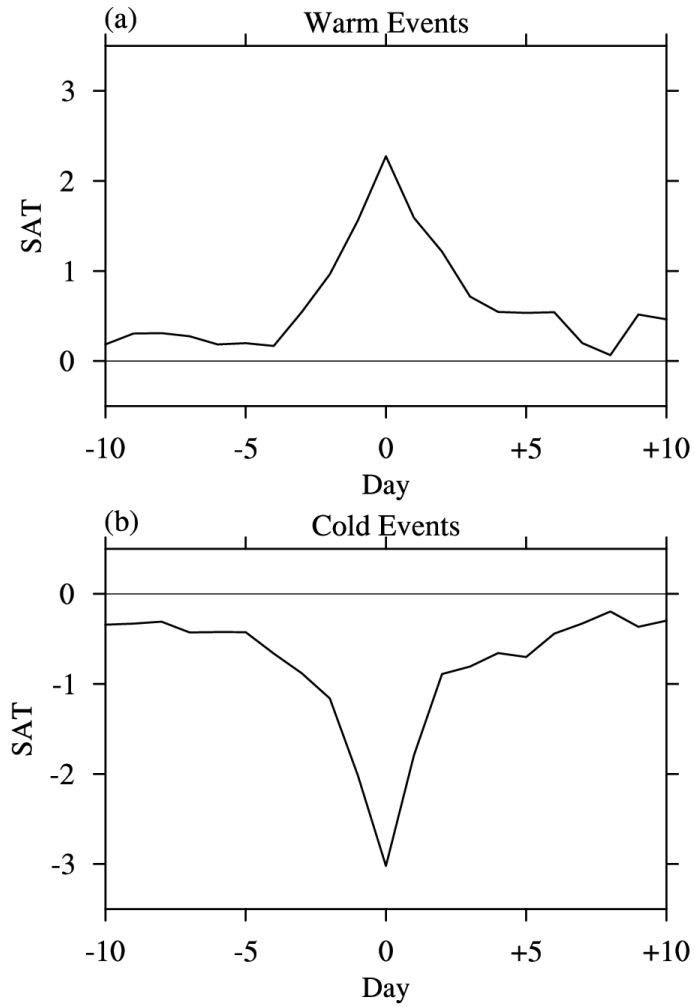
717

718

719

720

721



722

723 **Fig. 1** Time evolution of surface air temperature (SAT) anomalies (°C) at the Great

724 Wall Station during lag -10 to lag +10 days of (a) warm and (b) cold events.

725

726

727

728

729

730

731

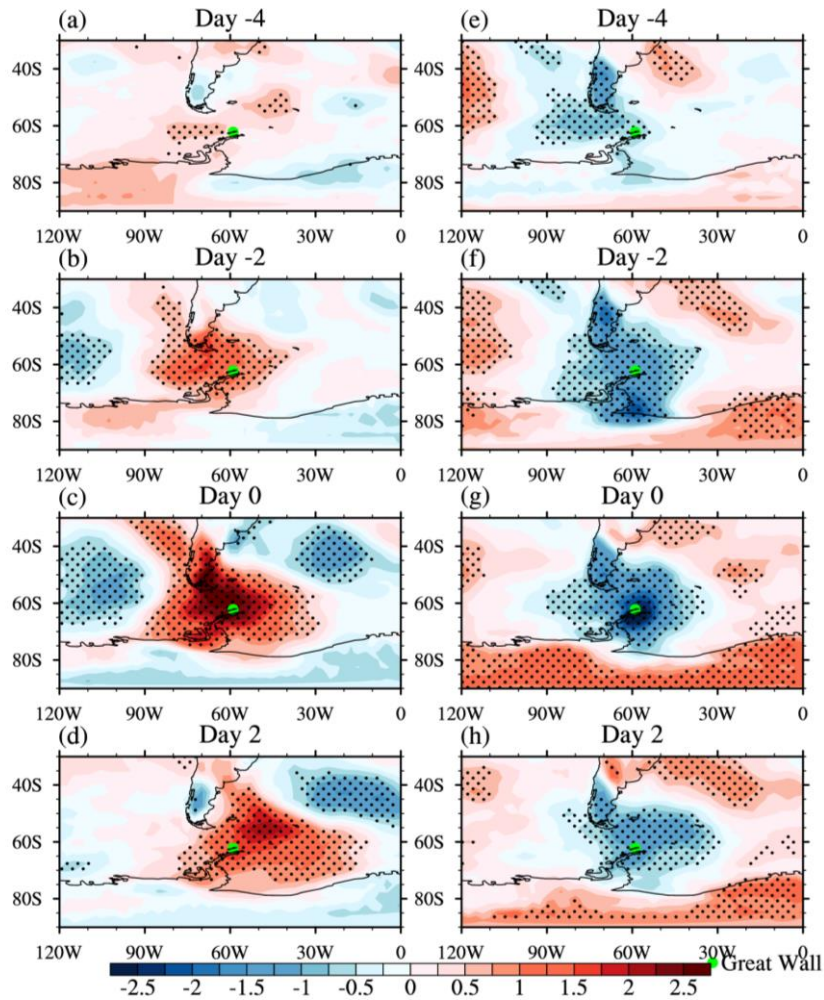
732

733

734

735

736



737

738 **Fig. 2** Composite SAT anomalies (°C) on days (a) -4, (b) -2, (c) 0 and (d) +2 of the

739 warm events. (e)-(h) are the same as (a)-(d) but for cold events. The dots indicate

740 anomalies significant at the 95% confidence level. The green dot indicates the

741 location of the Great Wall Station.

742

743

744

745

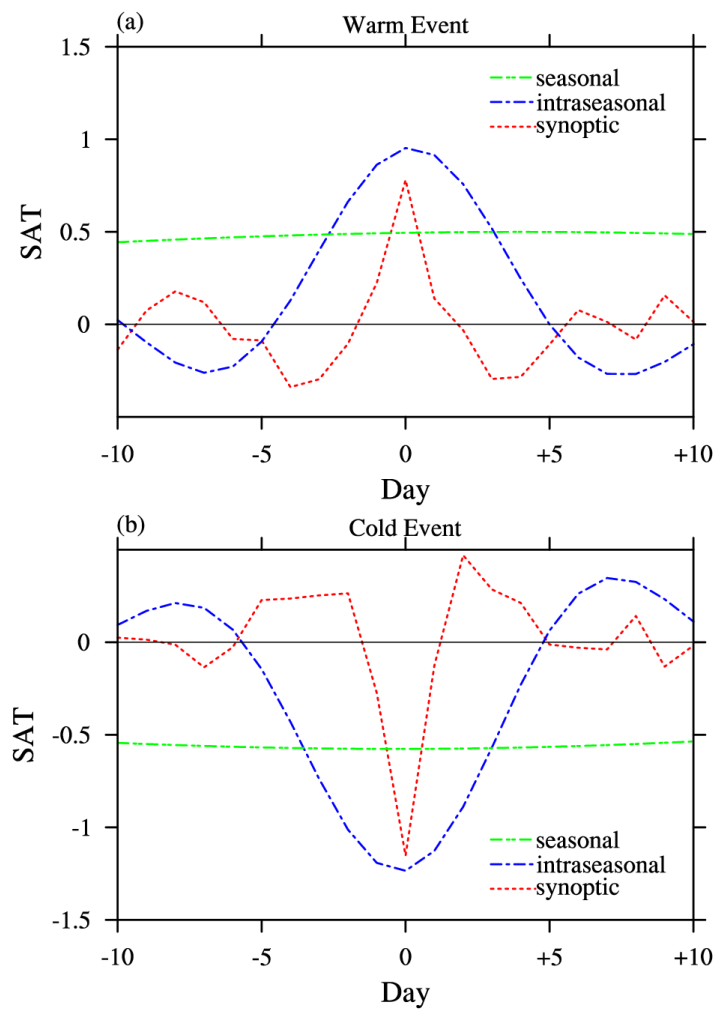
746

747

748

749

750



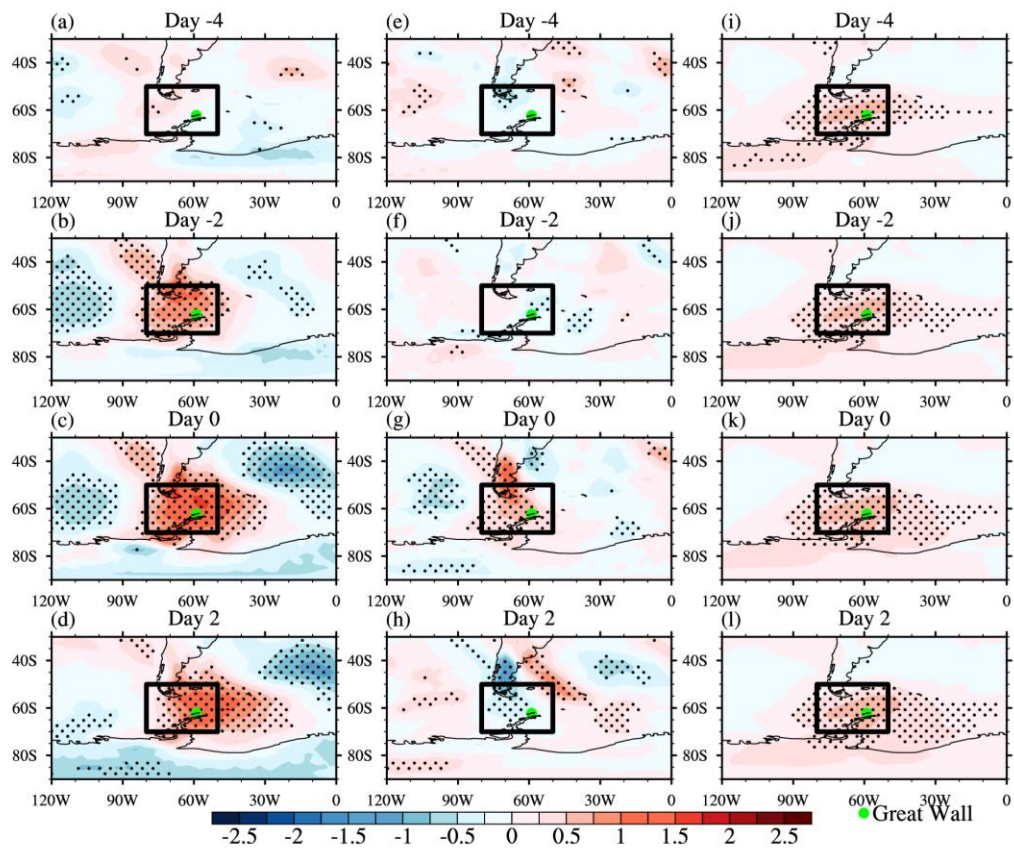
752

753 **Fig. 3** The same as Fig. 1 but for the synoptic, intraseasonal, and seasonal components

754

of SAT.

755



756

757 **Fig. 4** Composite anomalies of the intraseasonal component of SAT (°C) on days (a) -
 758 4, (b) -2, (c) 0 and (d) +2 of the warm events. (e)-(h) and (i)-(l) are the same as (a)-(d)
 759 but for the synoptic and seasonal components of SAT, respectively. The dots indicate
 760 anomalies significant at the 95% confidence level. The green dot indicates the
 761 location of the Great Wall Station.

762

763

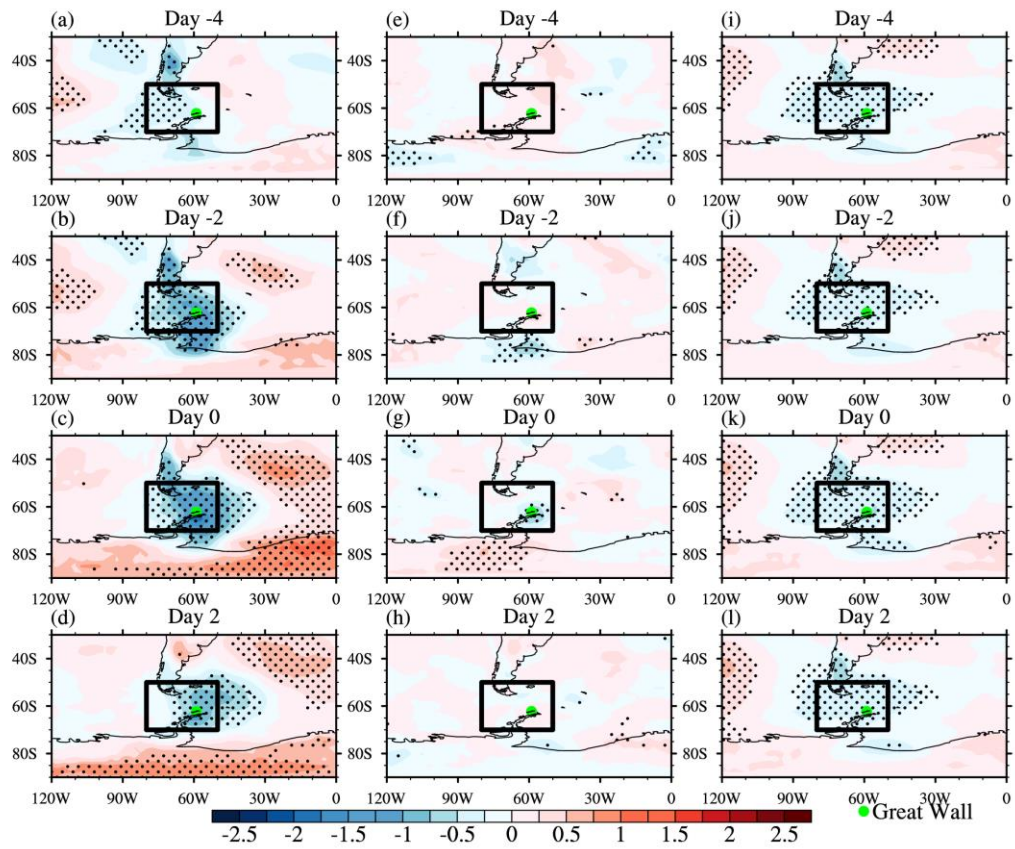
764

765

766

767

768



770

771

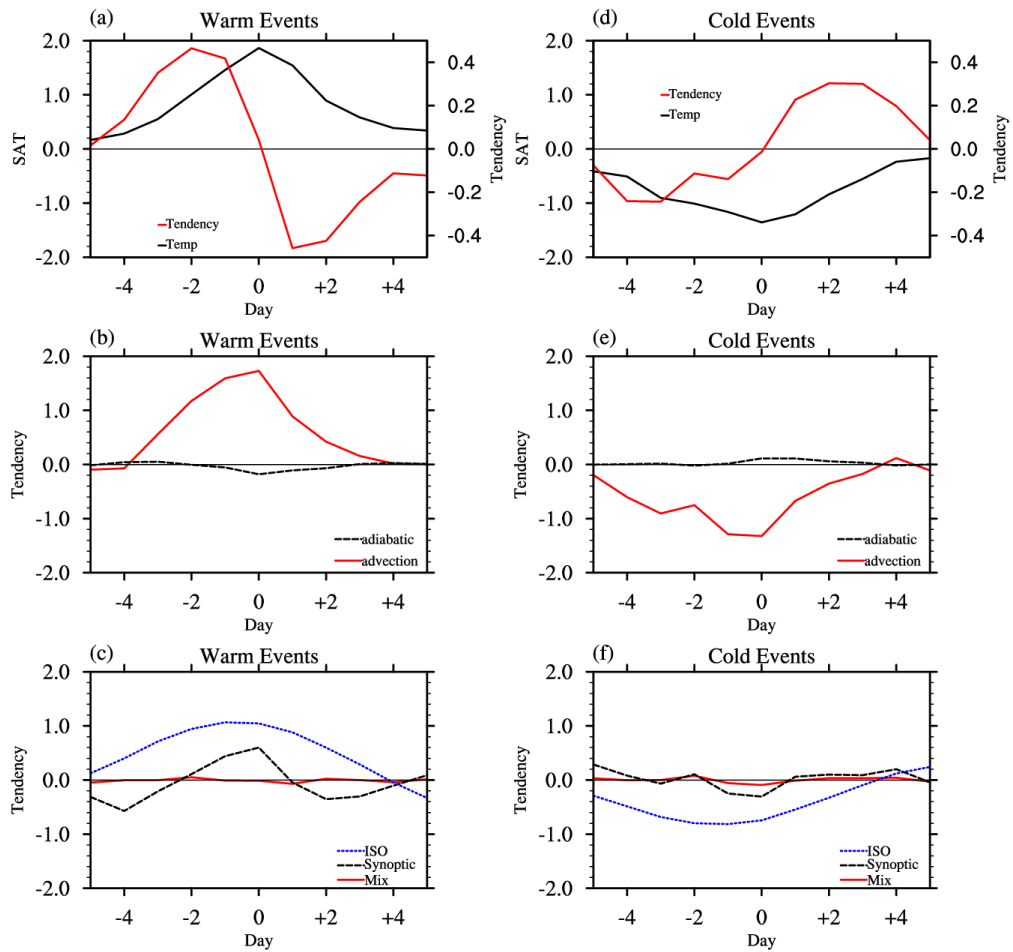
Fig. 5 The same as Fig. 4 but for the cold events.

772

773

774

775



776

777 **Fig. 6** Time evolution of the composite anomalies of (a) SAT (black line), SAT
 778 tendency (red line), (b) SAT tendency induced by advection (red line) and adiabatic
 779 (black line) terms and (c) SAT tendency caused by different parts of the advection
 780 term averaged over the Drake Passage (70°S – 50°S and 80°W – 50°W) during lag -5 to
 781 lag +5 days of the warm events. (d)-(f) are the same as (a)-(c) but for the cold events.

782

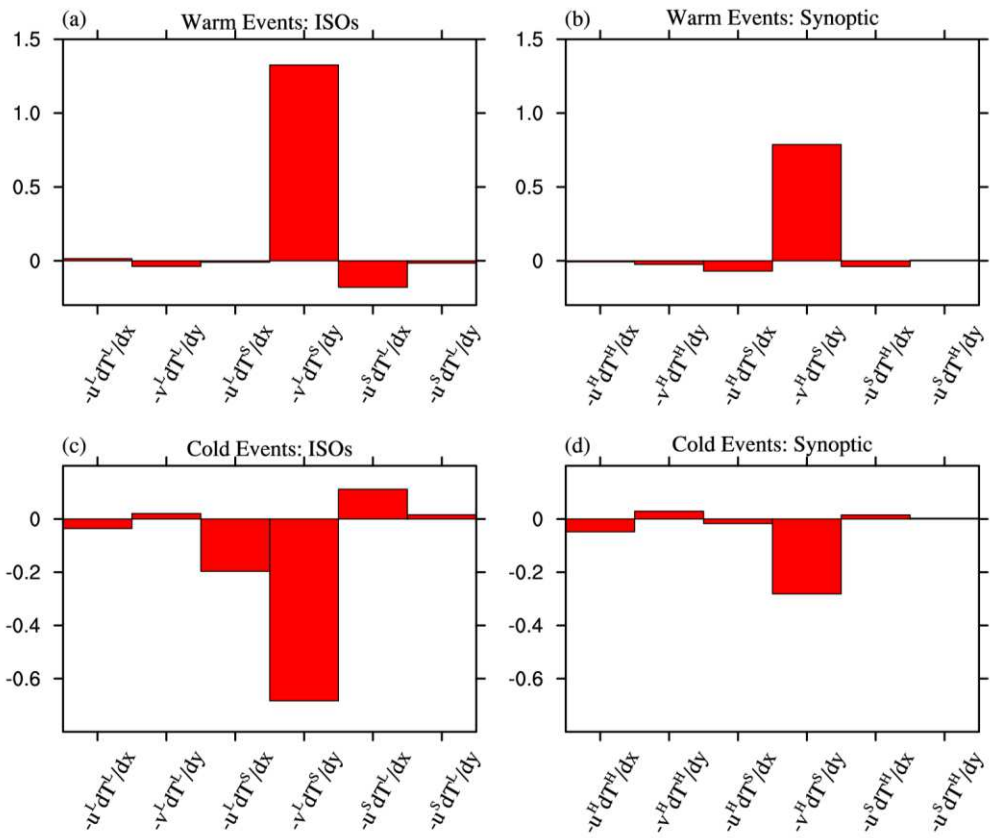
783

784

785

786

787



789

790 **Fig. 7** Different parts of advection terms associated with the (a), (c) ISOs and (b), (d)
 791 synoptic variations on lag 0 day of the warm and cold events, respectively.

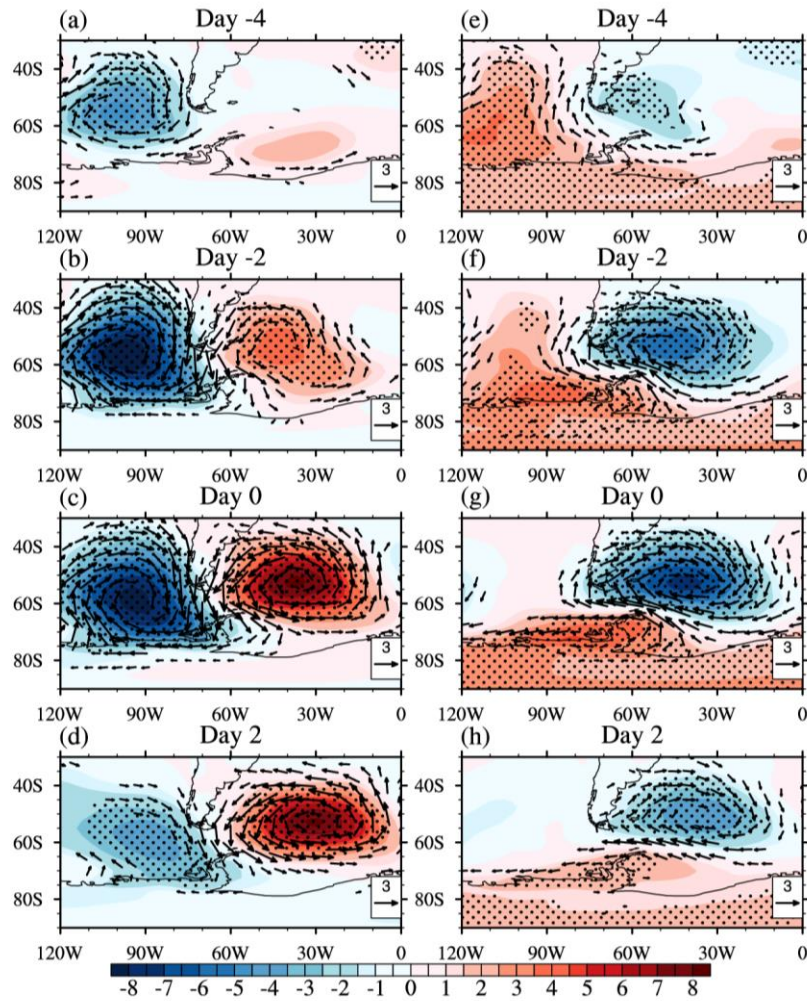
792

793

794

795

796



797

798 **Fig. 8** Composite anomalies of intraseasonal components of SLP (hPa) (shading) and

799 surface winds (ms^{-1}) (vectors) on days (a) -4, (b) -2, (c) 0 and (d) +2 of the warm

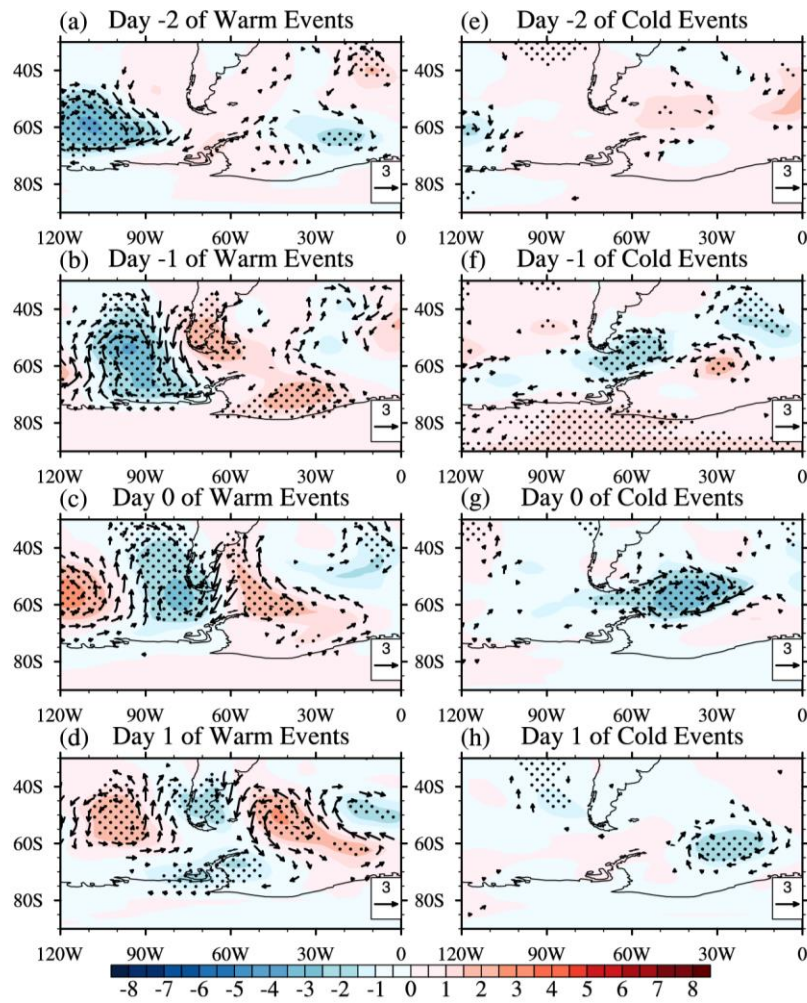
800 events. (e)-(h) are the same as (a)-(d) but for the cold events. The dots indicate

801 anomalies significant at the 95% confidence level.

802

803

804



805

806

Fig. 9 Composite anomalies of synoptic components of SLP (hPa) (shading) and surface winds (ms^{-1}) (vectors) on days (a) -2, (b) -1, (c) 0 and (d) +1 of the warm events. (e)-(h) are the same as (a)-(d) but for the cold events. The dots indicate

807

anomalies significant at the 95% confidence level.

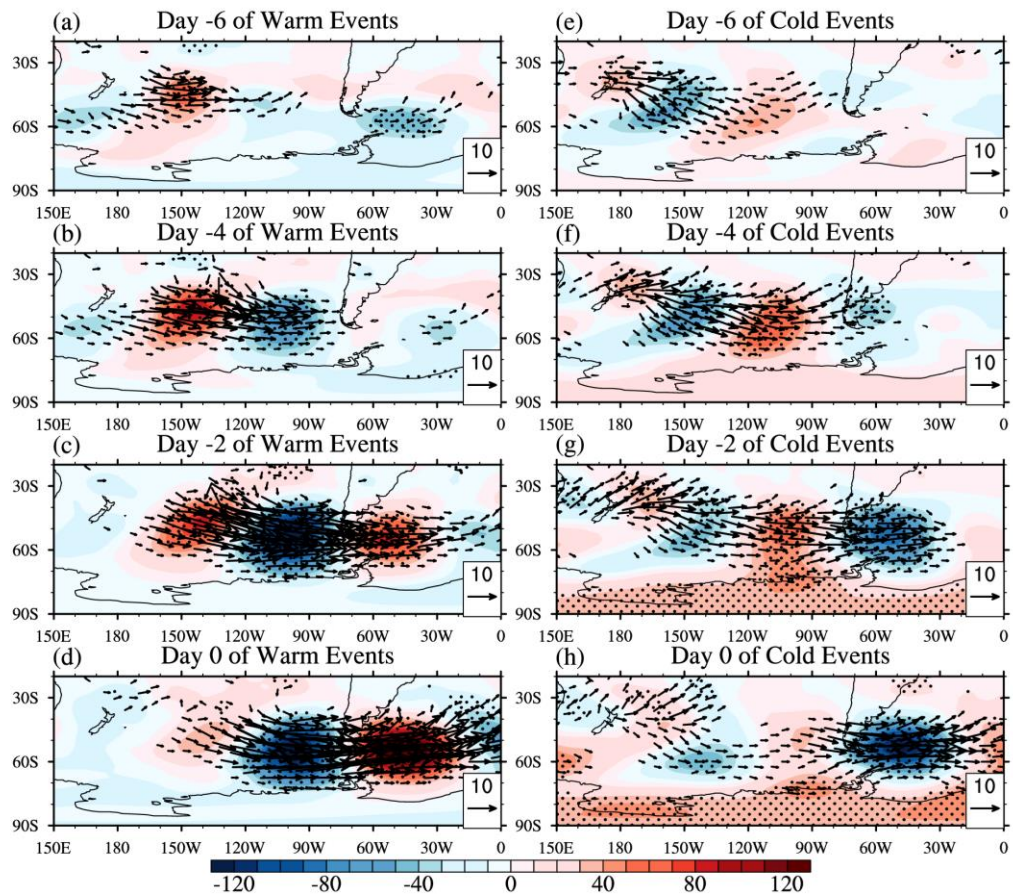
808

anomalies significant at the 95% confidence level.

809

810

811



812

813 **Fig. 10** Composite anomalies of the intraseasonal component of geopotential height

814 anomalies at 300 hPa (m) (shading) and the attendant wave activity flux (vector) on

815 days (a) -6, (b) -4, (c) -2 and (d) 0 of the warm events. (e)-(h) are the same as (a)-(d)

816 but for the cold events. The dots indicate anomalies significant at the 95% confidence

817 level.

818

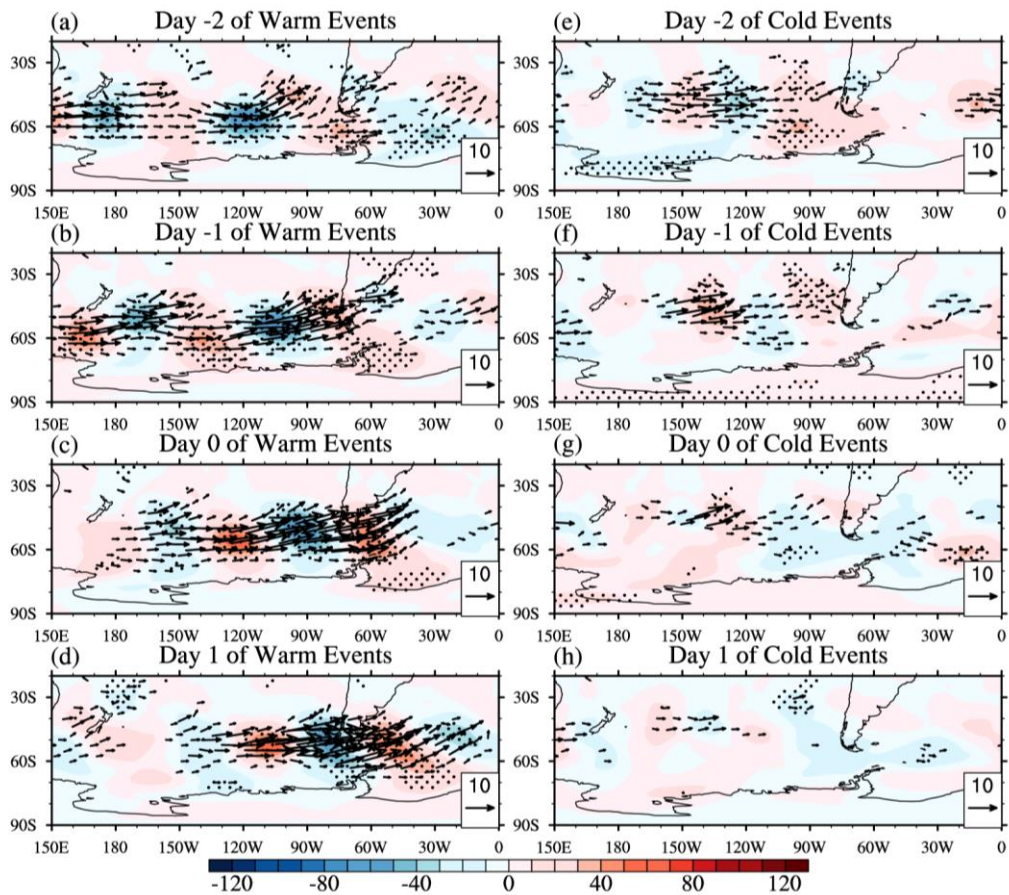
819

820

821

822

823



824

825 **Fig. 11** Composite anomalies of the synoptic component of geopotential height

826 anomalies at 300 hPa (m) (shading) and the attendant wave activity flux (vector) on

827 days (a) -2, (b) -1, (c) 0 and (d) +1 of the warm events. (e)-(h) are the same as (a)-(d)

828 but for the cold events. The dots indicate anomalies significant at the 95% confidence

829 level.

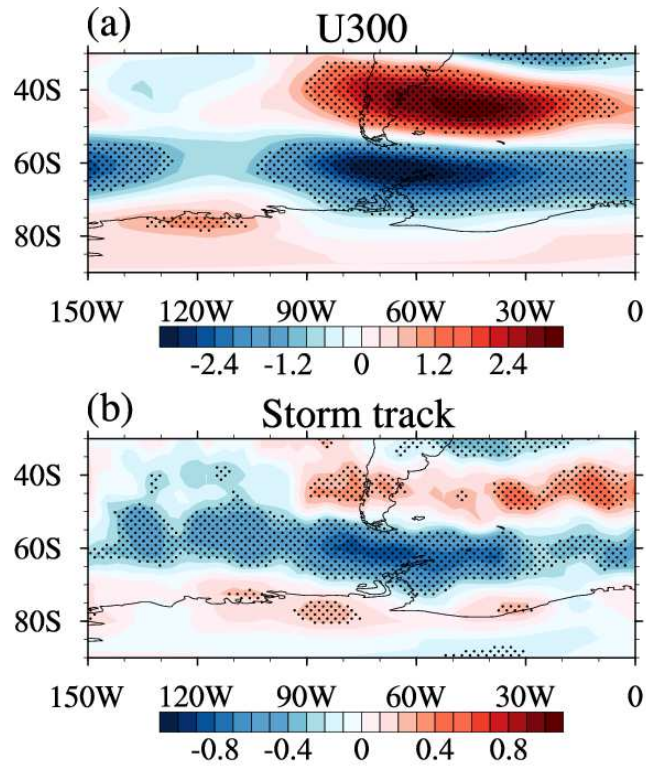
830

831

832

833

834



835

836 **Fig. 12** Composite anomalies of the seasonal component of (a) 300-hPa zonal wind

837 (ms^{-1}) and (b) 300-hPa storm track activity (m) for the cold events. The dots indicate

838 anomalies significant at the 95% confidence level.

839

840

841

842

843

844

845

846

847

848

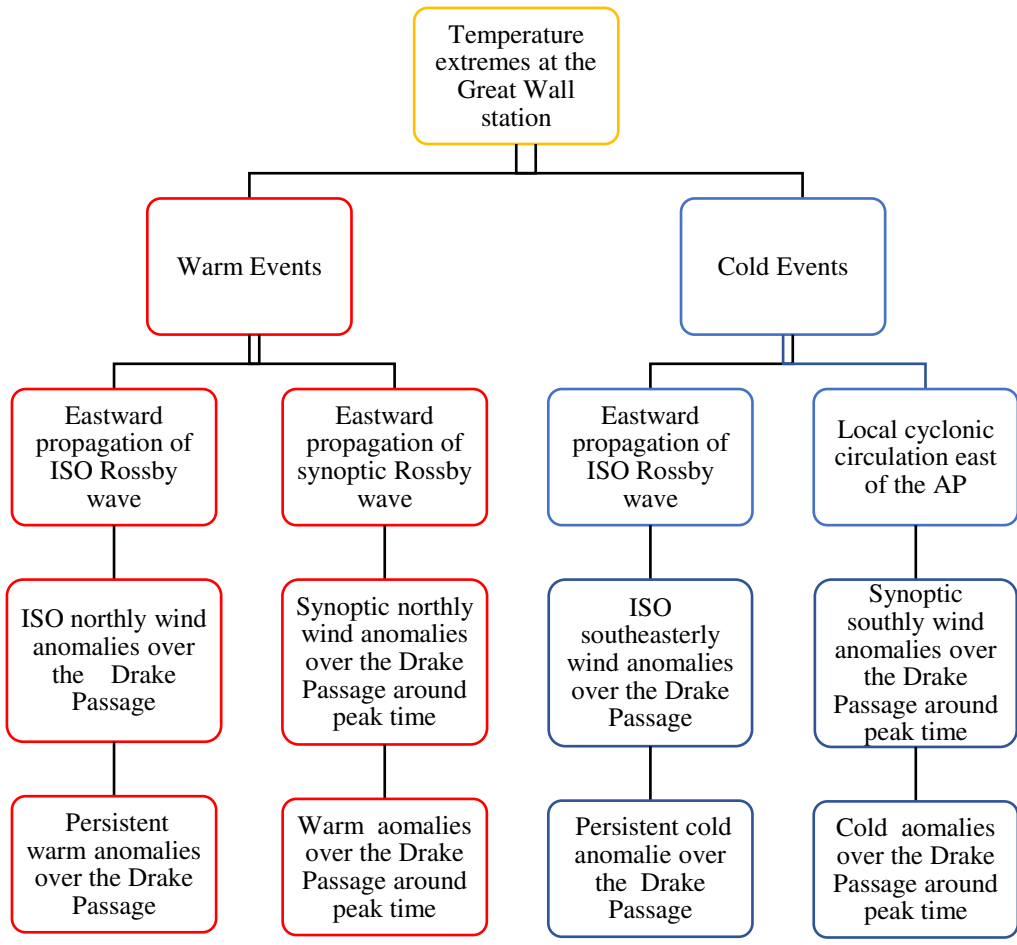
849

850

851

852

853



855

856

Fig. 13 Schematic illustration of the role of atmospheric flow in the formation

857

of summer temperature extremes at the Great Wall Station, Antarctic

858

Peninsula, during austral summer.

859

Figures

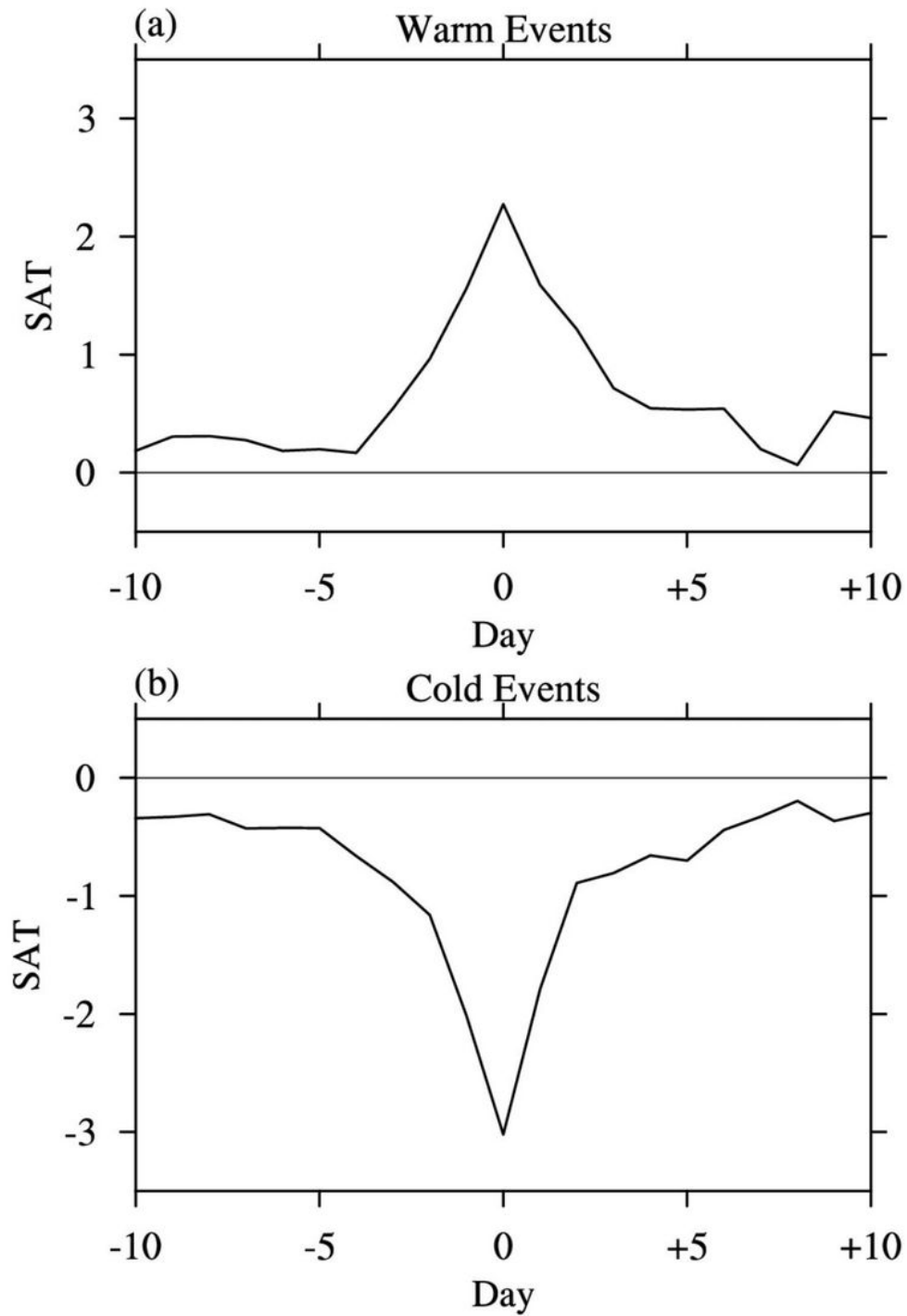


Figure 1

Time evolution of surface air temperature (SAT) anomalies ($^{\circ}\text{C}$) at the Great Wall Station during lag -10 to lag +10 days of (a) warm and (b) cold events.

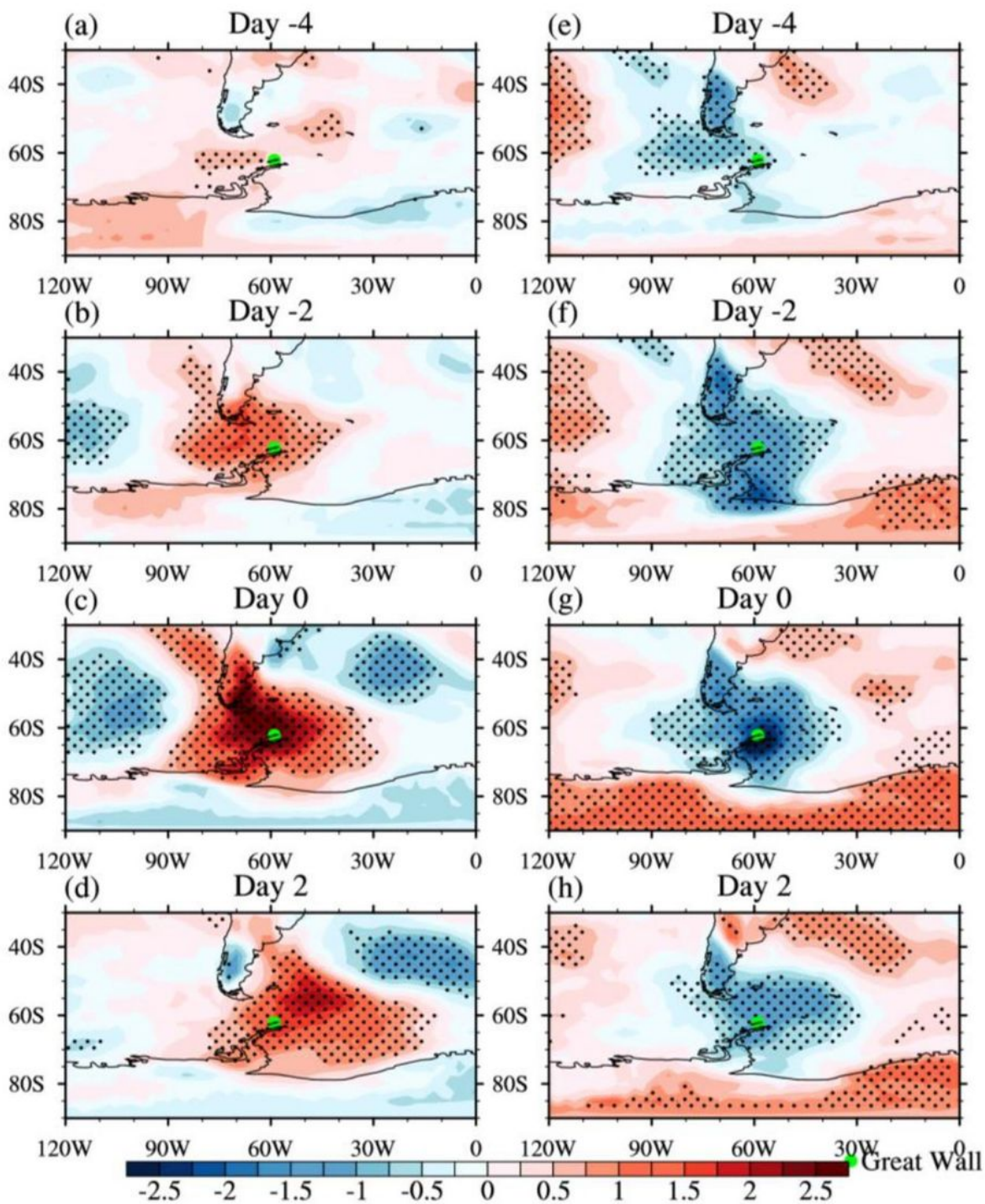


Figure 2

Composite SAT anomalies (°C) on days (a) -4, (b) -2, (c) 0 and (d) +2 of the warm events. (e)-(h) are the same as (a)-(d) but for cold events. The dots indicate anomalies significant at the 95% confidence level. The green dot indicates the location of the Great Wall Station.

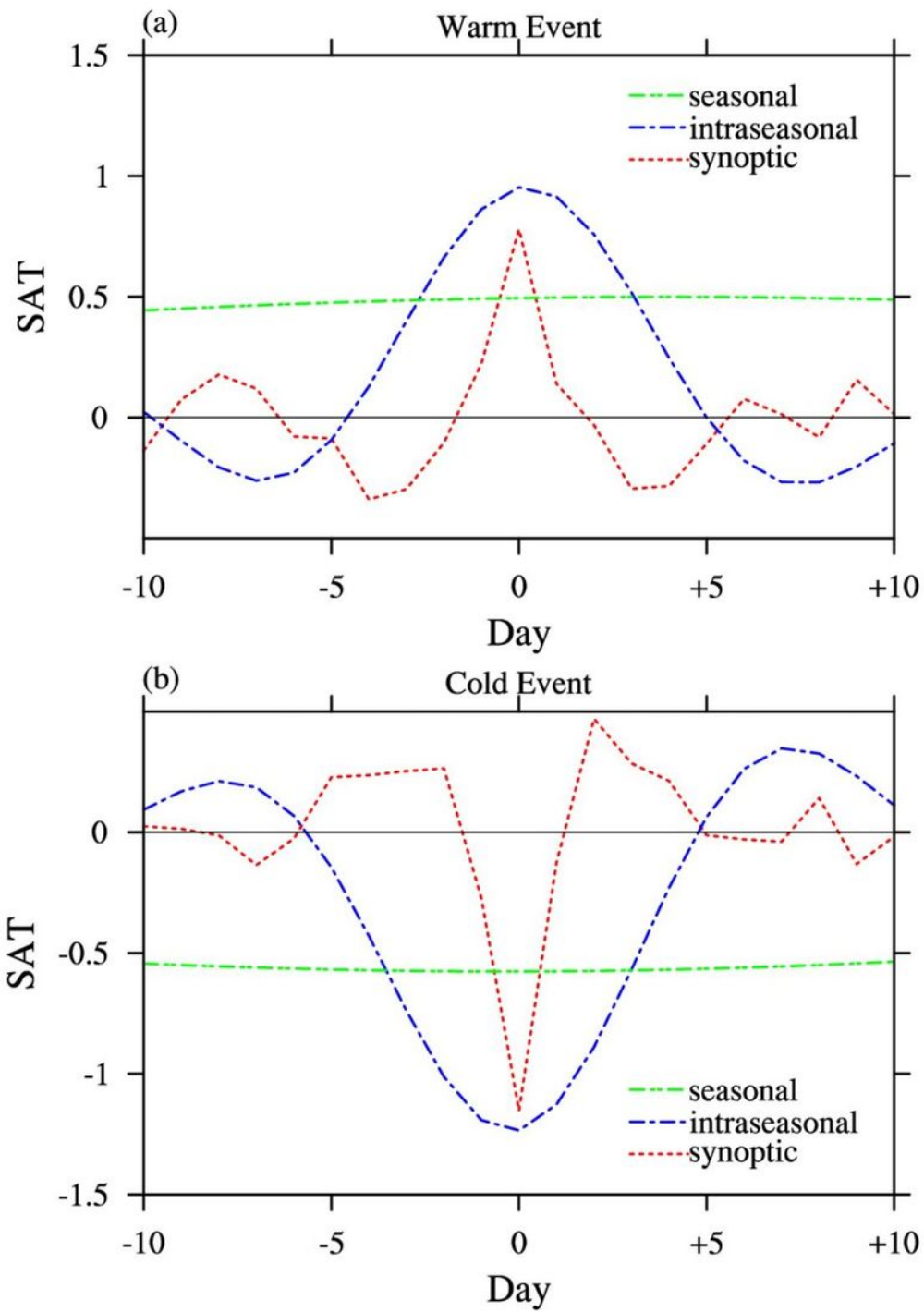


Figure 3

The same as Fig. 1 but for the synoptic, intraseasonal, and seasonal components of SAT.

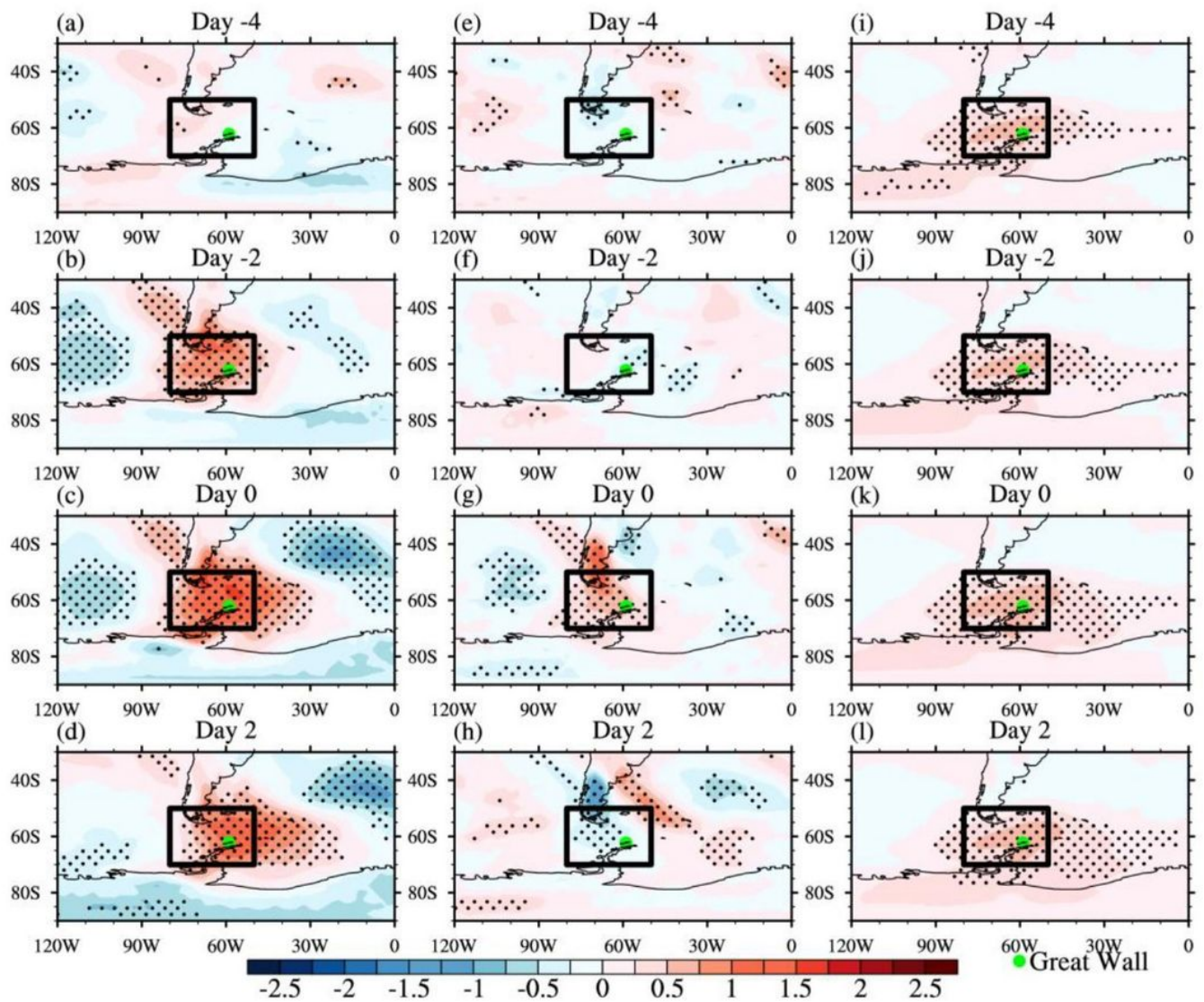


Figure 4

Composite anomalies of the intraseasonal component of SAT ($^{\circ}\text{C}$) on days (a) -4, (b) -2, (c) 0 and (d) +2 of the warm events. (e)-(h) and (i)-(l) are the same as (a)-(d) but for the synoptic and seasonal components of SAT, respectively. The dots indicate anomalies significant at the 95% confidence level. The green dot indicates the location of the Great Wall Station.

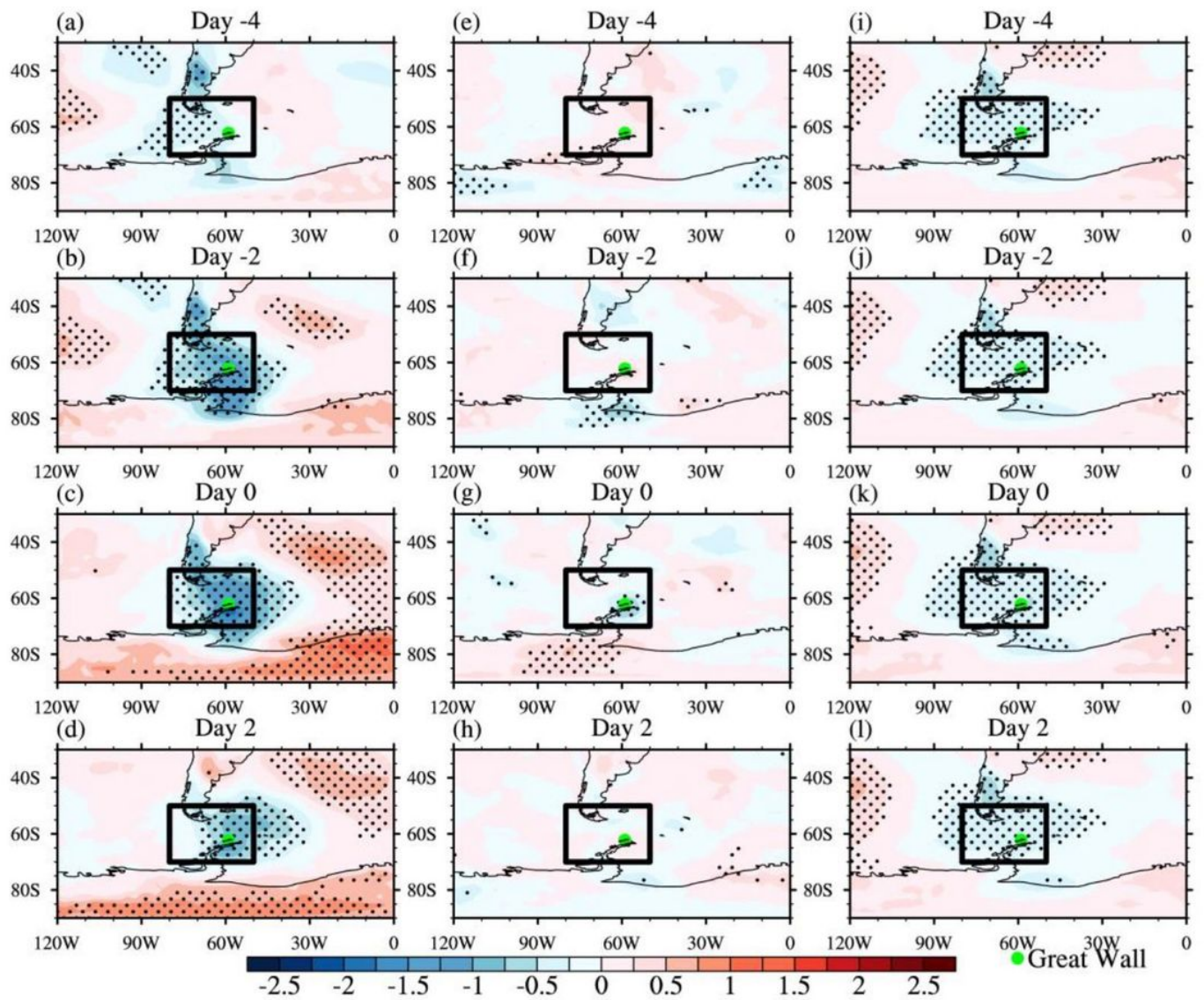


Figure 5

The same as Fig. 4 but for the cold events.

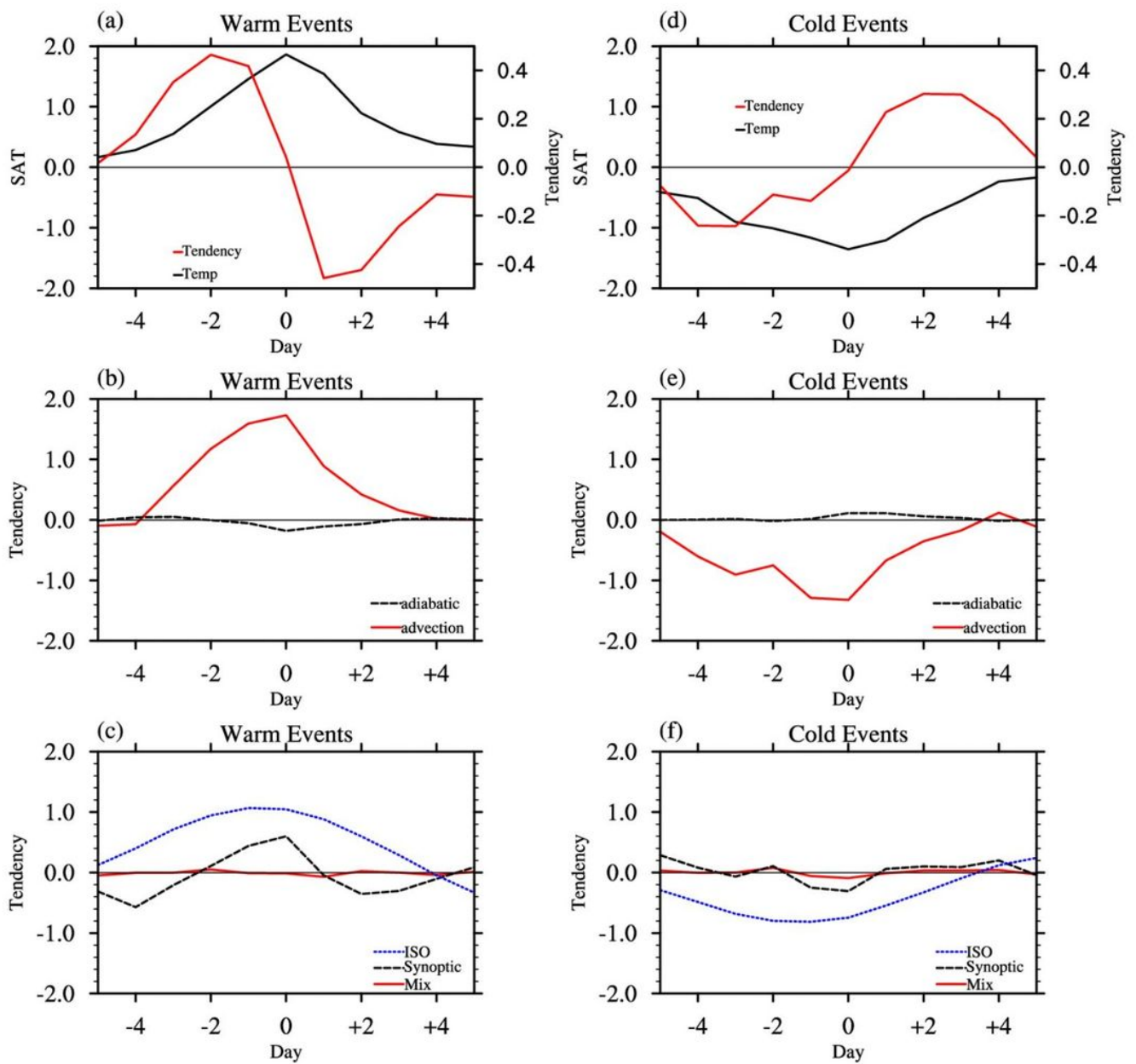


Figure 6

Time evolution of the composite anomalies of (a) SAT (black line), SAT tendency (red line), (b) SAT tendency induced by advection (red line) and adiabatic (black line) terms and (c) SAT tendency caused by different parts of the advection term averaged over the Drake Passage (70°S–50°S and 80°W–50°W) during lag -5 to lag +5 days of the warm events. (d)-(f) are the same as (a)-(c) but for the cold events.

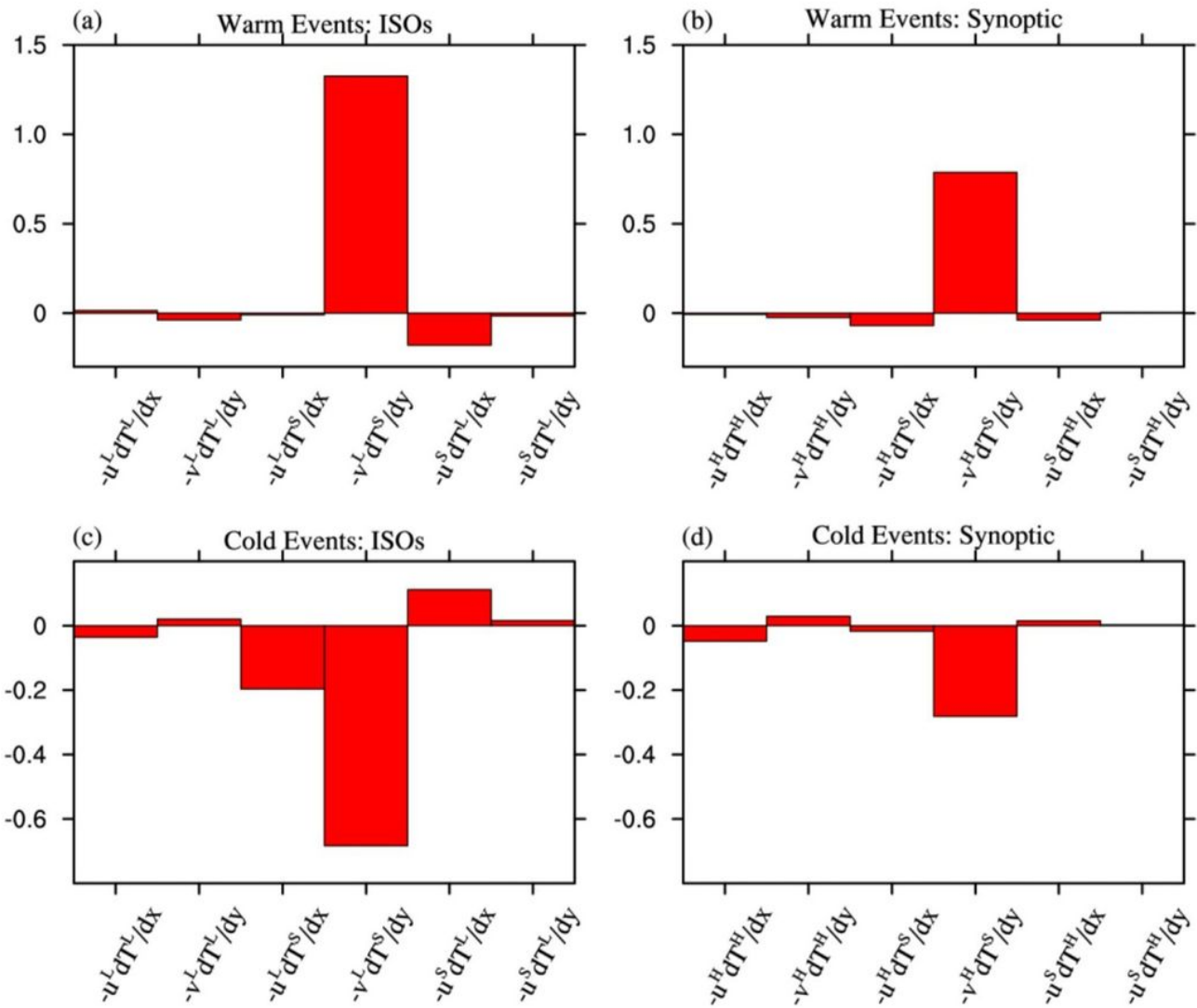


Figure 7

Different parts of advection terms associated with the (a), (c) ISOs and (b), (d) synoptic variations on lag 0 day of the warm and cold events, respectively.

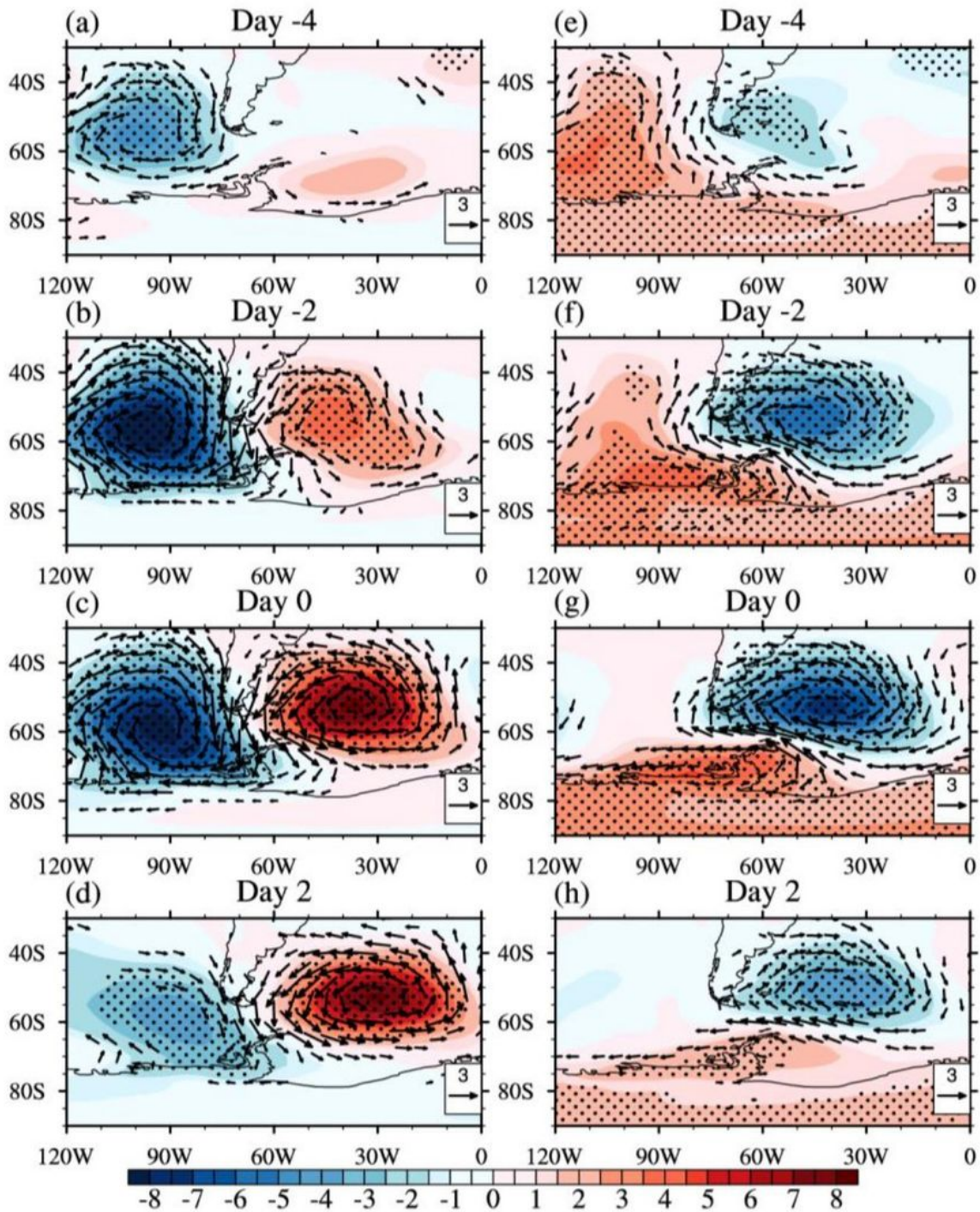


Figure 8

Composite anomalies of intraseasonal components of SLP (hPa) (shading) and surface winds (ms⁻¹) (vectors) on days (a) -4, (b) -2, (c) 0 and (d) +2 of the warm events. (e)-(h) are the same as (a)-(d) but for the cold events. The dots indicate anomalies significant at the 95% confidence level.

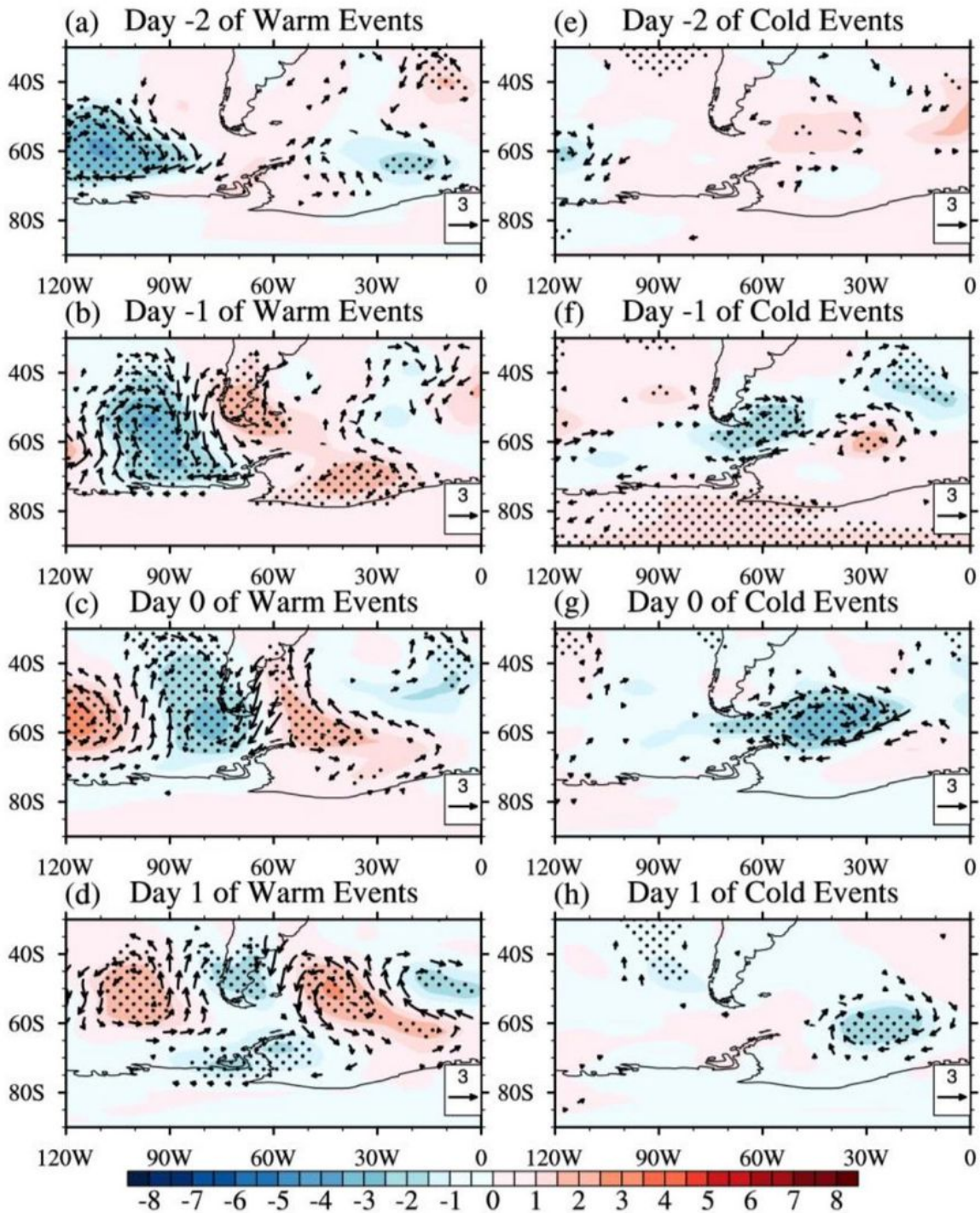


Figure 9

Composite anomalies of synoptic components of SLP (hPa) (shading) and surface winds (ms⁻¹) (vectors) on days (a) -2, (b) -1, (c) 0 and (d) +1 of the warm events. (e)-(h) are the same as (a)-(d) but for the cold events. The dots indicate anomalies significant at the 95% confidence level.

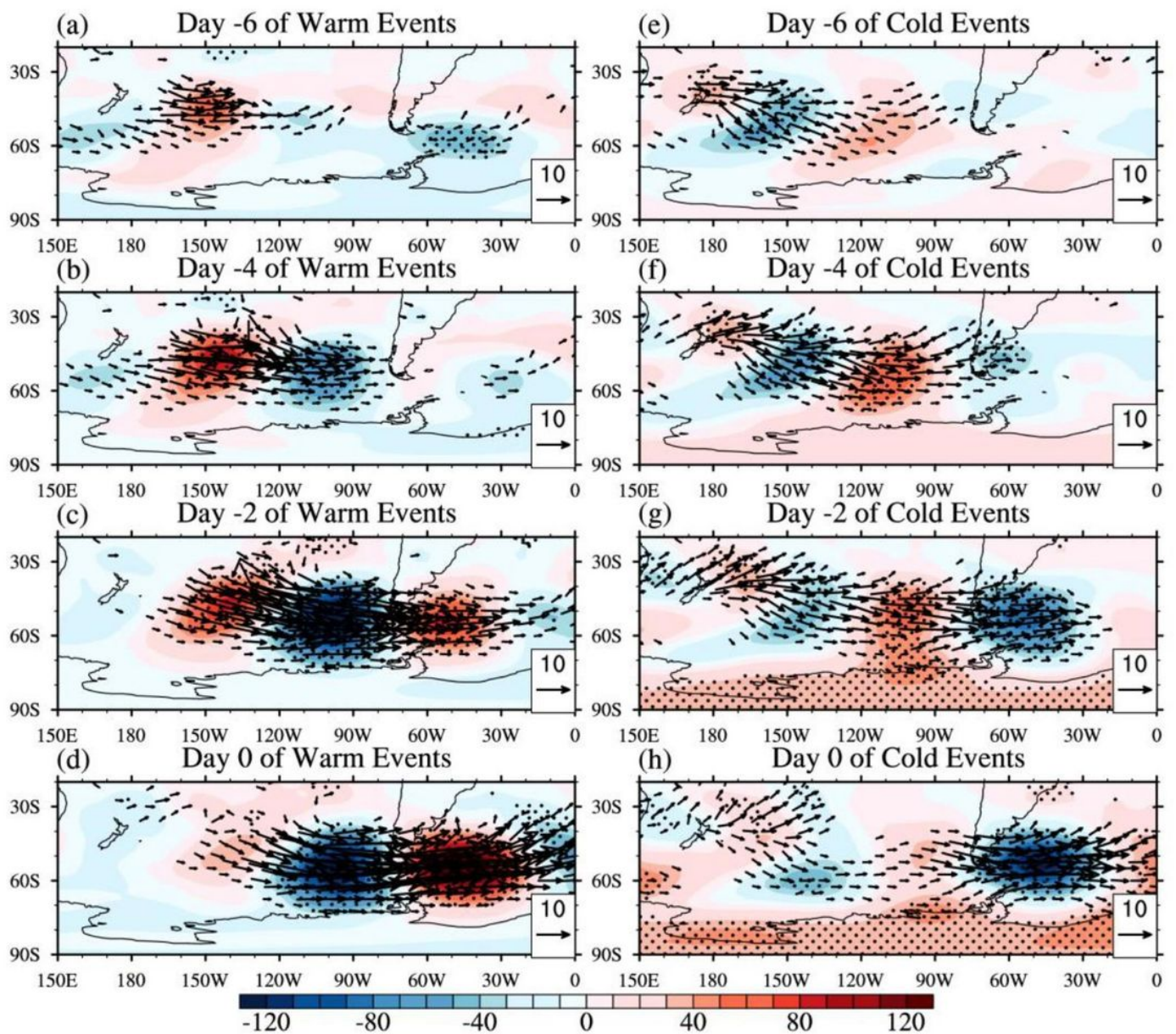


Figure 10

Composite anomalies of the intraseasonal component of geopotential height anomalies at 300 hPa (m) (shading) and the attendant wave activity flux (vector) on days (a) -6, (b) -4, (c) -2 and (d) 0 of the warm events. (e)-(h) are the same as (a)-(d) but for the cold events. The dots indicate anomalies significant at the 95% confidence level.

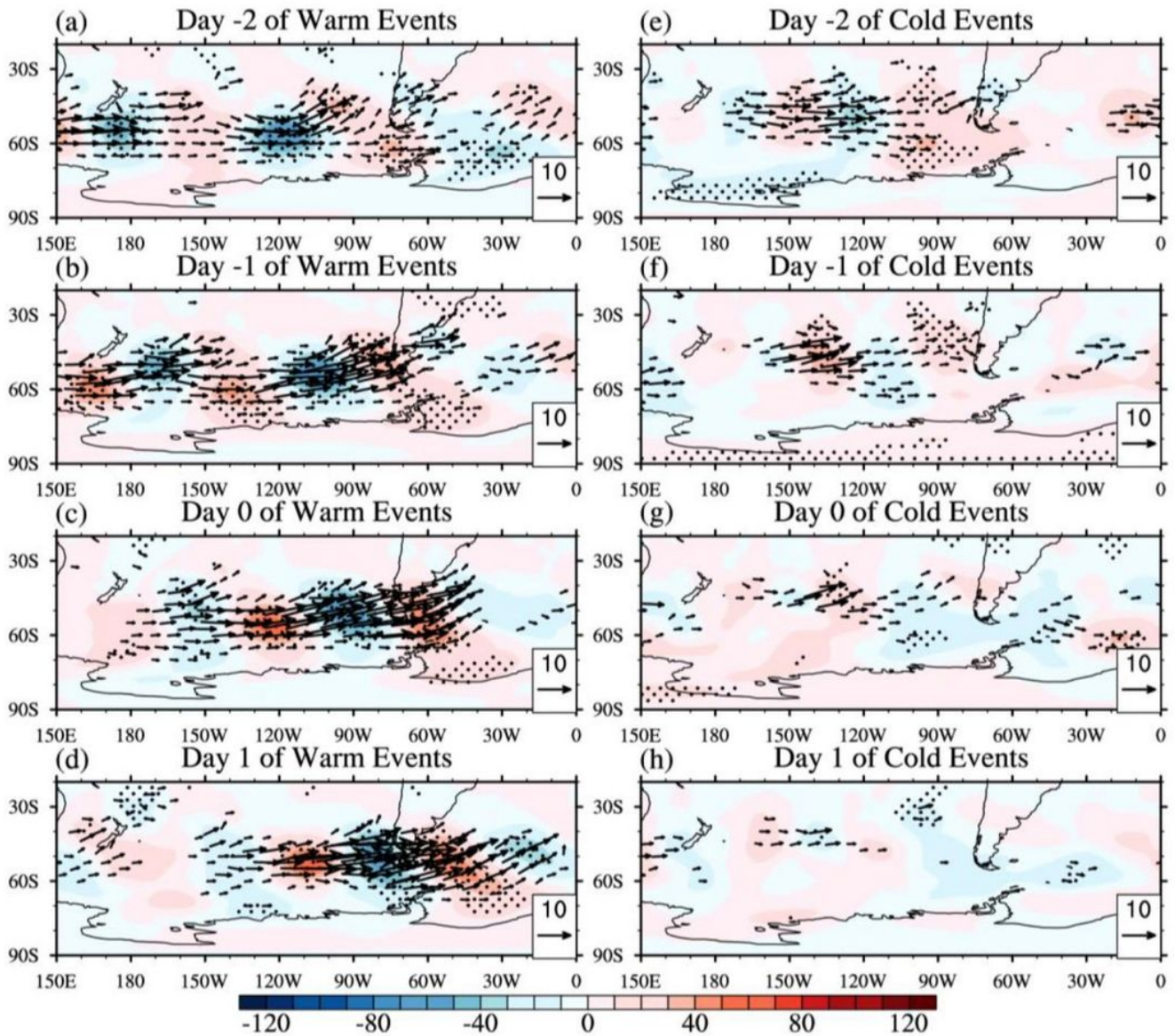


Figure 11

Composite anomalies of the synoptic component of geopotential height anomalies at 300 hPa (m) (shading) and the attendant wave activity flux (vector) on days (a) -2, (b) -1, (c) 0 and (d) +1 of the warm events. (e)-(h) are the same as (a)-(d) but for the cold events. The dots indicate anomalies significant at the 95% confidence level.

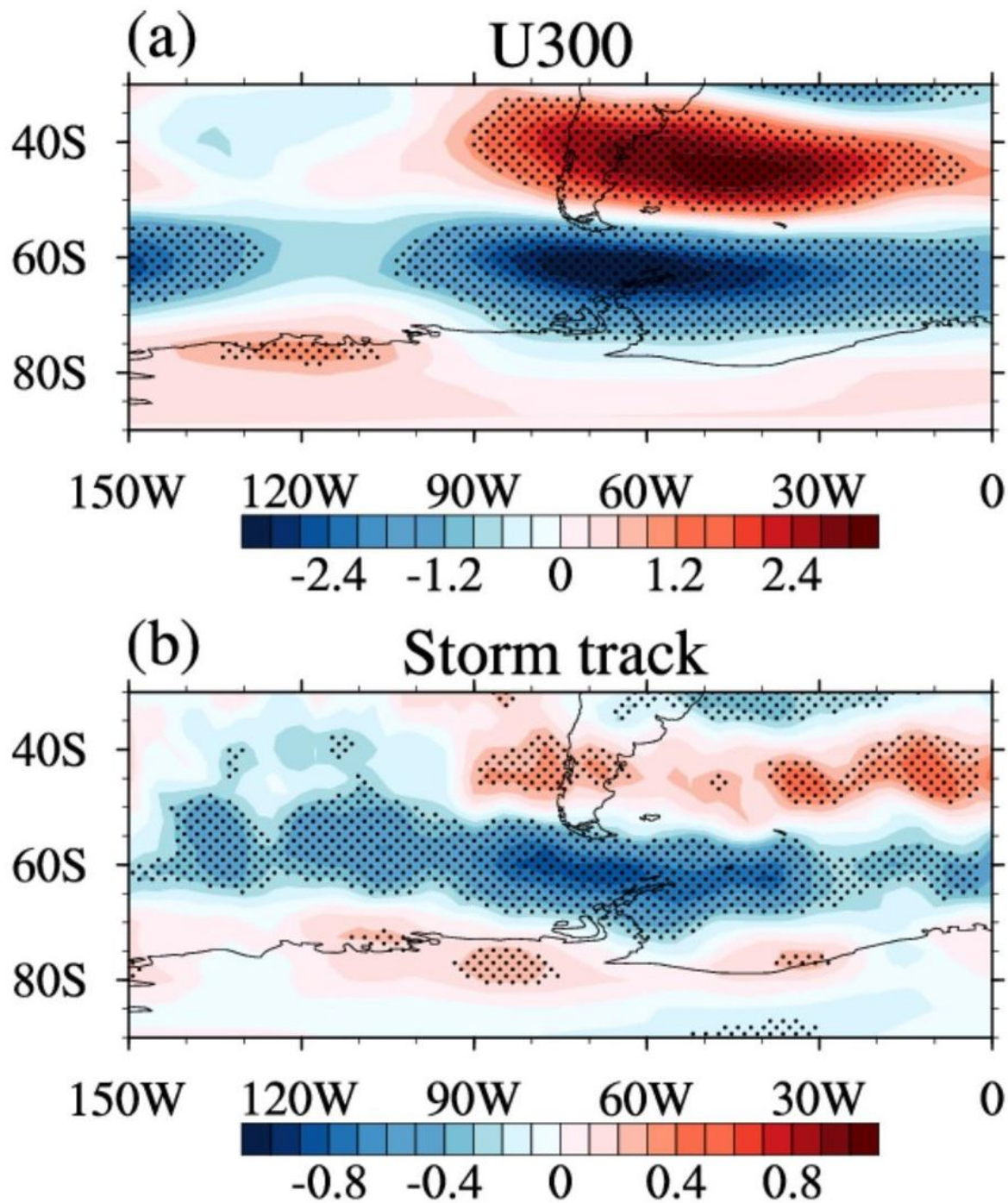


Figure 12

Composite anomalies of the seasonal component of (a) 300-hPa zonal wind (ms^{-1}) and (b) 300-hPa storm track activity (m) for the cold events. The dots indicate anomalies significant at the 95% confidence level.

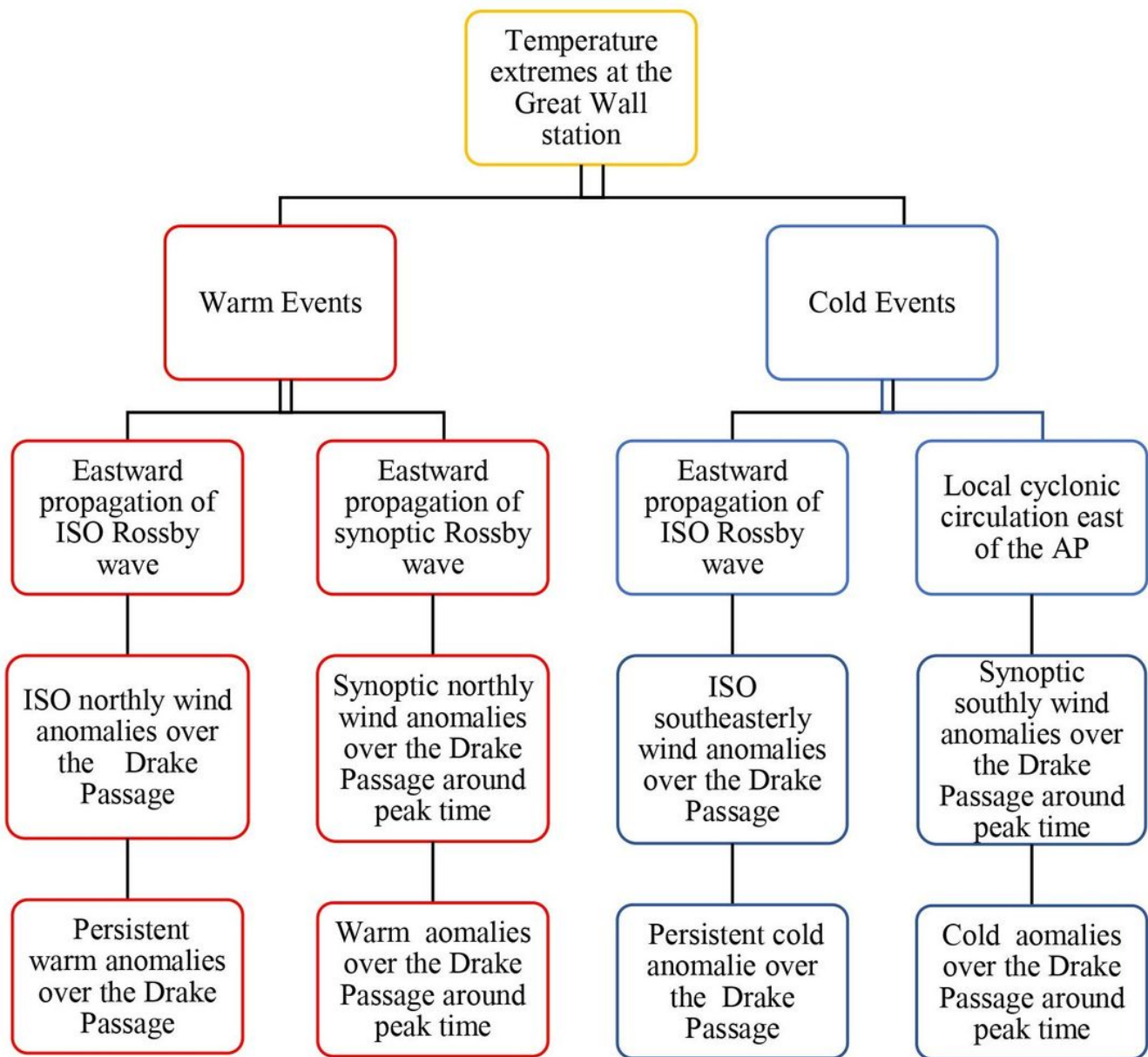


Figure 13

Schematic illustration of the role of atmospheric flow in the formation of summer temperature extremes at the Great Wall Station, Antarctic Peninsula, during austral summer.